STRUCTURE AND DYNAMICS OF THE BENTHIC BOUNDARY LAYER
ABOVE THE HATTERAS ABYSSAL PLAIN

by

ERIC ARTHUR D'ASARO

A.B. Harvard College (1976)
M.S. Harvard University (1976)

SUBMITTED IN PARTIAL FULFILLMENT
OF THE REQUIREMENTS FOR THE
DEGREE OF DOCTOR OF
PHILOSOPHY

at the

MASSACHUSETTS INSTITUTE OF TECHNOLOGY

and the

WOODS HOLE OCEANOGRAPHIC INSTITUTION

November, 1980

© Massachusetts Institute of Technology 1980

Signature of Author _____

Joint Program in Oceanography, Massachusetts Institute
of Technology-Woods Hole Oceanographic Institution, and
Department of Meteorology, Massachusetts Institute of
Technology, November, 1980.

Certified by _____ _____
                                          Laurence Armi
                                          Thesis Supervisor

Accepted by _____
            Chairman, Joint Oceanography Committee in Earth
            Sciences, Massachusetts Institute of Technology-
            Woods Hole Oceanographic Institution.

Abstract

The structure of the near-bottom velocity and density fields was observed for 3 months with a fixed velocity/temperature measuring array on the Hatteras Abyssal Plain. The velocity signal was examined for structure coherent with the observed mixed layers. Velocity fluctuations above 1 cph increase in energy near the bottom, expecially within bottom mixed layers. The frequency and energy of these fluctuations is consistent with the expected properties of boundary layer turbulence. The turbulence, as measured by these velocity fluctuations, is modulated on tidal and inertial time scales and extends intermittently throughout the bottom mixed layer. The clockwise near inertial velocity fluctuations, presumably due to internal waves, also show structure coherent with the observed mixed layers. Their energy decreases near the top of the mixed layer with little phase change. Within the mixed layer the phase begins to lead, with the phase increasing downward. The near inertial anticlockwise velocity fluctuations show far less coherence with the mixed layer structure; higher frequency internal wave band velocity fluctuations show very little coherence with the mixed layer structure. The characteristic boundary layer velocity signal in both the high frequency and near inertial bands commonly extends throughout the mixed layer, often significantly above the estimated turbulent Ekman layer height. These observations are inconsistent with a steady turbulent Ekman layer model of the boundary layer.

The interaction of the internal wave field and the benthic boundary layer above a flat bottom is investigated using a diagnostic model. Assuming the internal waves to be large compared with the boundary layer, the turbulent stresses acting on the waves and the work done by the stresses on the waves can be computed. The data indicates observable energy transfer only for near inertial waves. The boundary layer is estimated to absorb .004 - .025 ergs/cm^2/s from the near inertial internal wave field. This is far less than estimated by Leaman (1976) and suggests that the benthic boundary layer on a flat bottom plays a minor role in dissipating internal wave energy. This is also much less than the total energy dissipation in the boundary layer, suggesting that the boundary layer is primarily driven by low frequency motions. A simple slab model with a linearized quadratic drag law qualitatively explains the observed boundary layer near inertial clockwise velocity structure and energy flux. Thesis Advisor: Laurence Armi.

Contents

Acknowledgments

Chapter 1.   Introduction

Observations close to the ocean bottom show a distinct region, the benthic boundary layer, in which bottom generated shear turbulence appears to be dynamically significant.   Bowden (1978) reviews previous work on this subject.   Oceanographically, the benthic boundary layer may be significant in damping oceanic motions, and mixing the oceanic interior.   Fluid dynamically, it is a useful example of a turbulent boundary layer influenced by rotation and stratification, but without significant heating or cooling.   Over large regions of the ocean a bottom mixed layer, vertically uniform in potential temperature, salinity and light scattering (Armi and Millard, 1976; Caldwell, 1976; Weatherly and Niiler, 1974) is present.   This layer is believed to be mixed by the boundary layer turbulence.   In a recent study Armi and D'Asaro (1980) describe the three dimensional density structure of the benthic boundary layer over the Hatteras Abyssal Plain in the western North Atlantic. The bottom mixed layer is found to extend 5-60 m above the abyssal plain with typical heights of 20-30 m.   The layer exhibits considerable variability on time scales of days and longer, and horizontal space scales of tens of kilometers and larger.   Multiple mixed layers are common.   These are presumably caused by the intrusion of the bottom mixed layer into the interior.   Benthic fronts are also observed.   The observed density variations at a fixed point appear to be primarily due to advection of horizontal density structure by the velocity field.

This thesis will analyze the velocity data taken during the same experiment.   Studies of the benthic boundary layer have often concen-

6

trated on the structure of the mean flow and turbulence in the bottom part of the boundary layer. In this region the benthic boundary layer appears similar to a two dimensional turbulent boundary layer and the velocity profile can be used to estimate the bottom stress. (Wimbush and Munk, 1970; Weatherly, 1972; Caldwell and Chriss, 1979). The measurements described here are not sufficiently close to the bottom to duplicate these calculations. They instead span the entire mixed layer, extending into the interior, so that the velocity structures associated with the mixed layer can be observed.

The turbulent Ekman layer provides a useful starting point for the analysis of the mixed layer velocity structure. The unstratified tur-bulent boundary layer driven by a steady geostrophic flow in a rotating coordinate system will here be called a turbulent Ekman layer. Its structure has been investigated theoretically using asymptotic matching (Csanady, 1967; Blakadar and Tennekes, 1968), laboratory simulations (Caldwell et al., 1972; Howroyd and Slawson, 1975), and the analysis of atmospheric and oceanic boundary layers under neutral conditions (Lettau, 1950; McPhee and Smith, 1976). One result of these studies is that the turbulent Ekman layer extends only to a height of roughly $\delta_{EK} \sim .4 \ u*/f$ where $\rho u*^2$ is the wall stress. The turbulent stresses and velocity fluctuations diminish rapidly above this height (Caldwell et al., 1972; McPhee and Smith, 1976). The benthic boundary layer is certainly more complex than a turbulent Ekman layer. One of the main aims of this thesis is determining the relevance of the turbulent Ekman layer and related models to the benthic boundary layer.

This thesis divides into two sections by content. Chapters 3 - 6 describe the observed mixed layer velocity structures. High frequency (chapter 4) and near inertial frequency (chapter 5) motions, which show the strongest structure are emphasized. These results are discussed in chapter 6. Chapters 7 - 10 analyze the near inertial motions using a diagnostic model of the internal wave/boundary layer interaction which allows the energy flux between the waves and the boundary layer to be computed. This interaction is then modeled using a simple slab model (chapter 9) and the results discussed (chapter 10).

Chapter 2.   The experiment and the instruments

A 3-month time series, May 18, 1977 to August 18, 1977, of

velocity and temperature was measured by a bottom mooring (Figure 1) de-

ployed on the Hatteras Abyssal Plain near 28°N, 70° 30'W by the Moored

Array Project of the Woods Hole Oceanographic Institution (W.H.O.I.).

The Hatteras Abyssal Plain is extremely flat with a slope of only

2×10^{-4} over hundreds of kilometers (Bush, 1976). The mooring

(W.H.O.I. 621) contained vector-averaging current meters (VACM) spaced

so as to span the bottom mixed layer. These sampled average velocity

and temperature every 7 1/2 minutes. A detailed description of the ex-

periment and the instrument calibration can be found in (Spencer,

D'Asaro and Armi, 1981).

The VACM instruments used in this experiment employ a Savonius

rotor and a vane to measure horizontal current (McCullough, 1975).

Bryden (1976) estimates an rms VACM direction bias of 2°. The measured

currents, however, show consistent directional differences larger than

this. A more detailed analysis (Spencer, D'Asaro and Armi, 1981) reveals

that instruments 1 and 4 are consistently 7° clockwise of instruments 2

and 3 from early June up to July 19. During this period the mooring

rotation, as measured by the VACM compasses is minimal. On July 19 and

20 the mooring orientation twice changes abruptly. Instrument 2, for

example, undergoes a net rotation of approximately 180° in less than

the sampling interval. The directional differences disappear after

July 20. This strongly suggests that the shears resulting from these
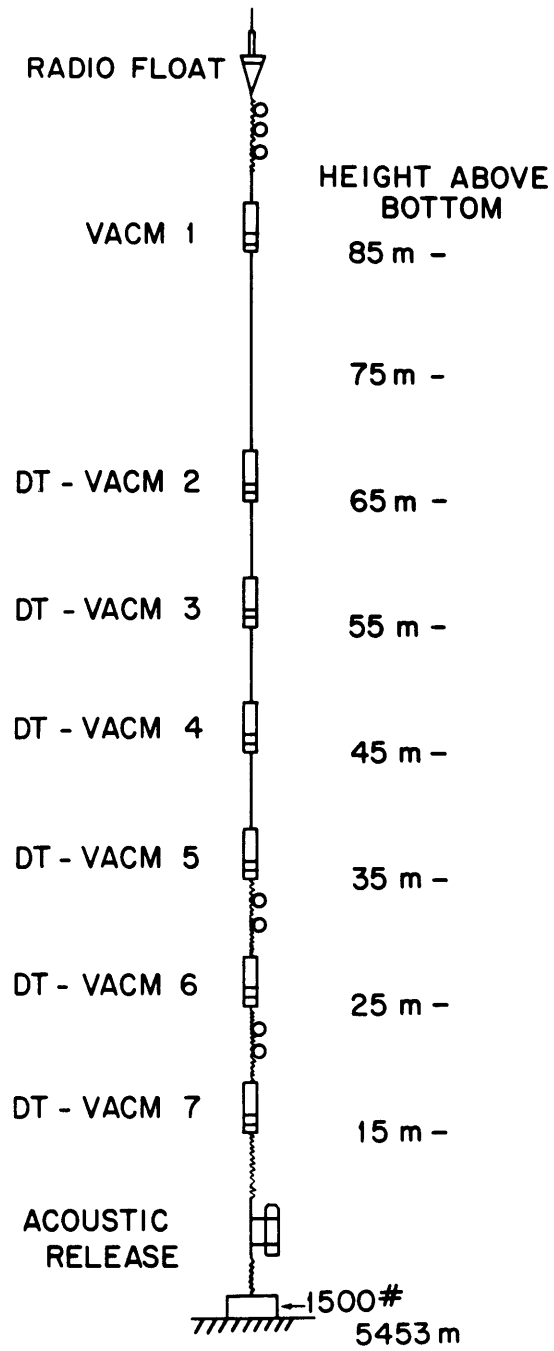
Figure 1

Mooring diagram. All vector-averaging current meters (VACM) measure vector mean current and temperature.

directional differences should be interpreted as instrumental errors of unknown origin. The VACMs in this experiment are therefore considered to have possible direction biases of up to 7° per pair, with this bias likely to be variable in time. These biases dominate the low frequency shears observed in this experiment, and make their scientific interpretation difficult.

The measured VACM temperature variations have a precision of better than a millidegree ($\pm 10^{-3}$°C). The absolute temperature is, however, less accurately measured and has been calibrated in situ as described in Armi and D'Asaro (1980) and Spencer, D'Asaro and Armi (1981). The correlation between salinity and potential temperature in this region, as determined by both historical measurements (MODE Group, 1978) and extensive CTD measurements during this experiment, is exact to within the salinity measurement error. Thus temperature alone gives a measurement of density at least as accurate as temperature and salinity together. Potential temperature differences will thus be interpreted as potential density differences throughout this paper using the formula $g\Delta\rho/\rho = .1\Delta\theta$ (Armi and D'Asaro, 1980).

Chapter 3. Spectral analysis

Figure 2 shows the horizontal kinetic energy spectra from all 7 instruments. These spectra are similar to those from other measurements in this area showing peaks at the inertial and tidal frequencies with a red spectrum at higher frequencies. The normalized energy at .2 cph, 3 $cm^2/s^2/cph^2$, is within the range found by Wunsch (1976) for western North Atlantic measurements. The spectral slope at .2 cph, approximately -3, is steeper than the typical slope of -1.7 found by Wunsch (1976). Figure 3 shows the horizontal kinetic energy spectrum from the 55 m instrument, here divided into clockwise and anticlockwise components (Calman, 1978). The clockwise energy is larger than the anticlockwise energy between the inertial and Väisälä frequency, as is typical of previous measurements (Fu, 1980).

Several features of the mean velocity spectra in figure 2 show distinct changes across the array. The near bottom instruments measure significantly more horizontal kinetic energy at frequencies above 1 cph. In chapter 4 this will be attributed to bottom generated turbulent velocity fluctuations. The near bottom instruments also measure significantly less horizontal kinetic energy near the inertial frequency. In chapter 8 this is attributed to turbulent stresses within the mixed layer. In both cases the energy level varies monotonically with distance from the bottom. Except at these frequencies the mean spectra from various instruments do not significantly differ.
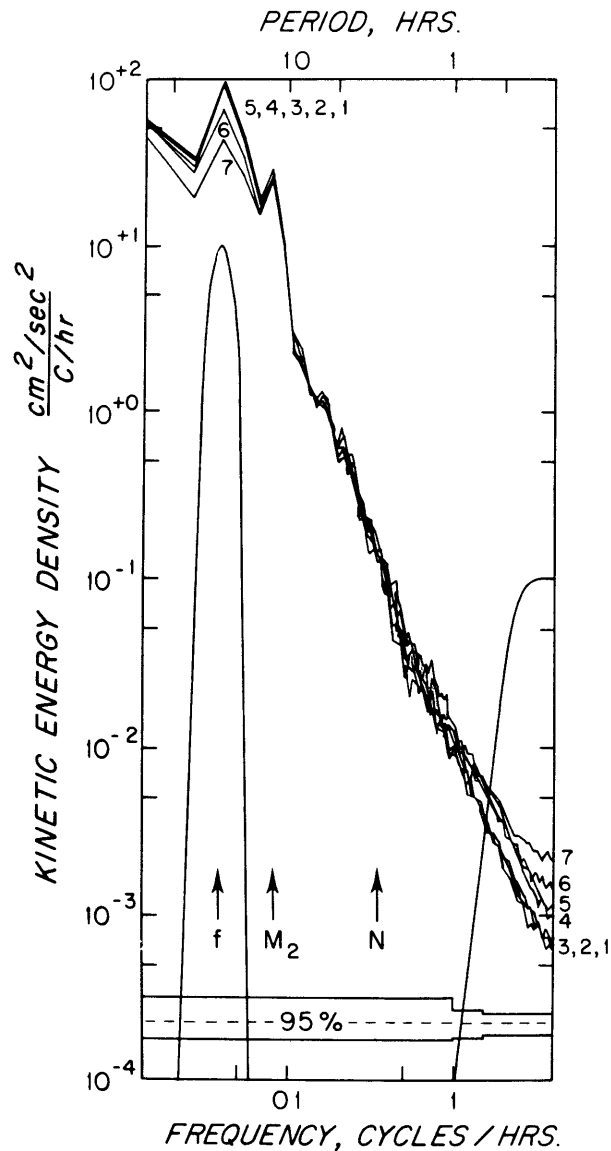
Figure 2

Horizontal kinetic energy spectra from all seven instruments. Labels
refer to instrument numbers (refer to figure 1). Each spectrum is the
average of 38 Hanned, overlapped pieces; higher frequencies are band
averaged. The 95% confidence limits and the inertial (f), M_2 tidal
and approximate Väisälä (N) frequencies are shown. The frequency re-
sponse of the digital filters used to compute the near inertial and high
pass velocity signals are shown.
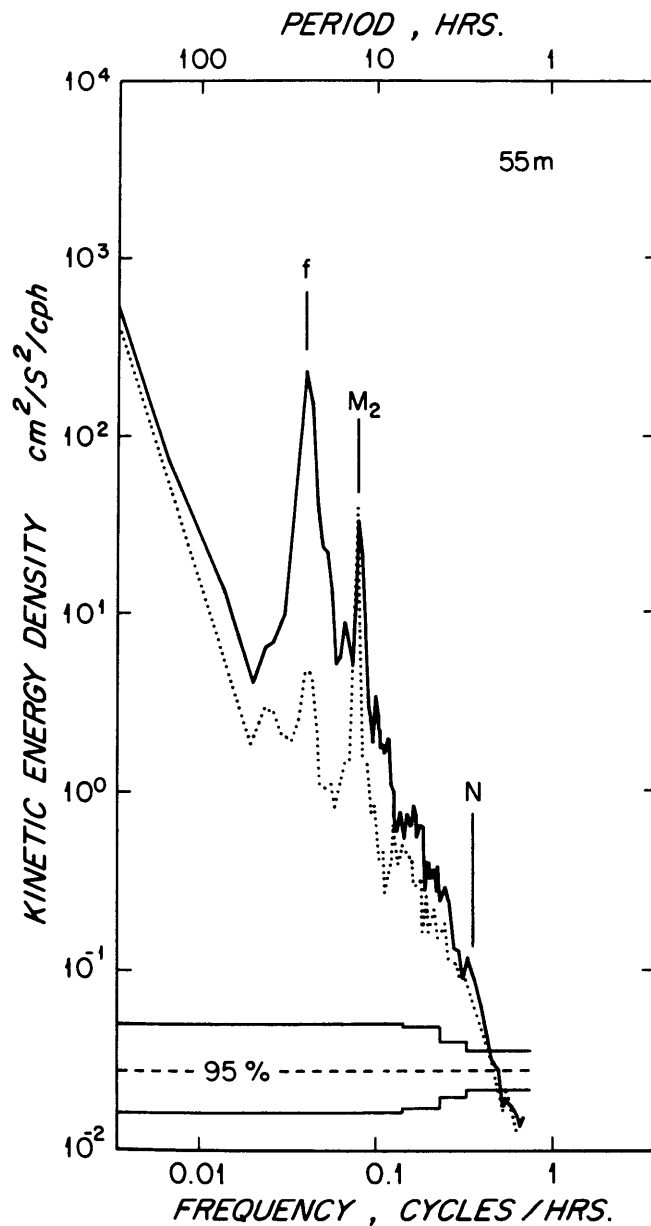
Figure 3

Clockwise (solid) and anticlockwise (dotted) kinetic energy spectra for
55 m instrument. Each spectrum is the average of 13 Hanned overlapped
pieces with higher frequencies band averaged. The 95% confidence limits
and the inertial (f), M_2 tidal, and approximate Väisälä (N) fre-
quencies are shown.

14

Figure 4 shows the east/east and north/north cross spectra between

instruments 3(55 m) and 7(15 m). Instrument 7 is in a bottom mixed

layer for 60 per cent of the record, while 3 never is. The coherence

for both components is high at tidal and inertial frequencies and drops

to below the 95 per cent significance level above the local Väisälä

frequency. The only significantly non-zero phases in figure 4 occur

at inertial and tidal frequencies. At the inertial frequency the

boundary layer leads the interior by about 25°. Similar results were

found by Hayes (1980) and Kundu (1976). Chapter 7 shows that these

phases are much larger than would be expected for internal waves alone

and must therefore be attributed to boundary layer effects.

Significantly, the vertical temperature coherences (not shown) in

this experiment are below the 95 per cent significance level at most

frequencies, for separations greater than 30 m. This is in marked

contrast to measurements in the oceanic interior, where the temperature

coherences are much higher than velocity coherences (Briscoe, 1975).

This is clearly due to the strong temperature signals, associated with

the bottom mixed layer, which are not present in the interior.

Each mean spectrum shown in figures 2 and 3 is the average of

measurements from a particular instrument at a fixed height above the

bottom. The mixed layer, however, varies greatly in height, so that any

particular near bottom instrument is sometimes within the mixed layer

and sometimes above it. Averaging over measurements at a fixed height

obscures any structure associated with the mixed layer. An alternative
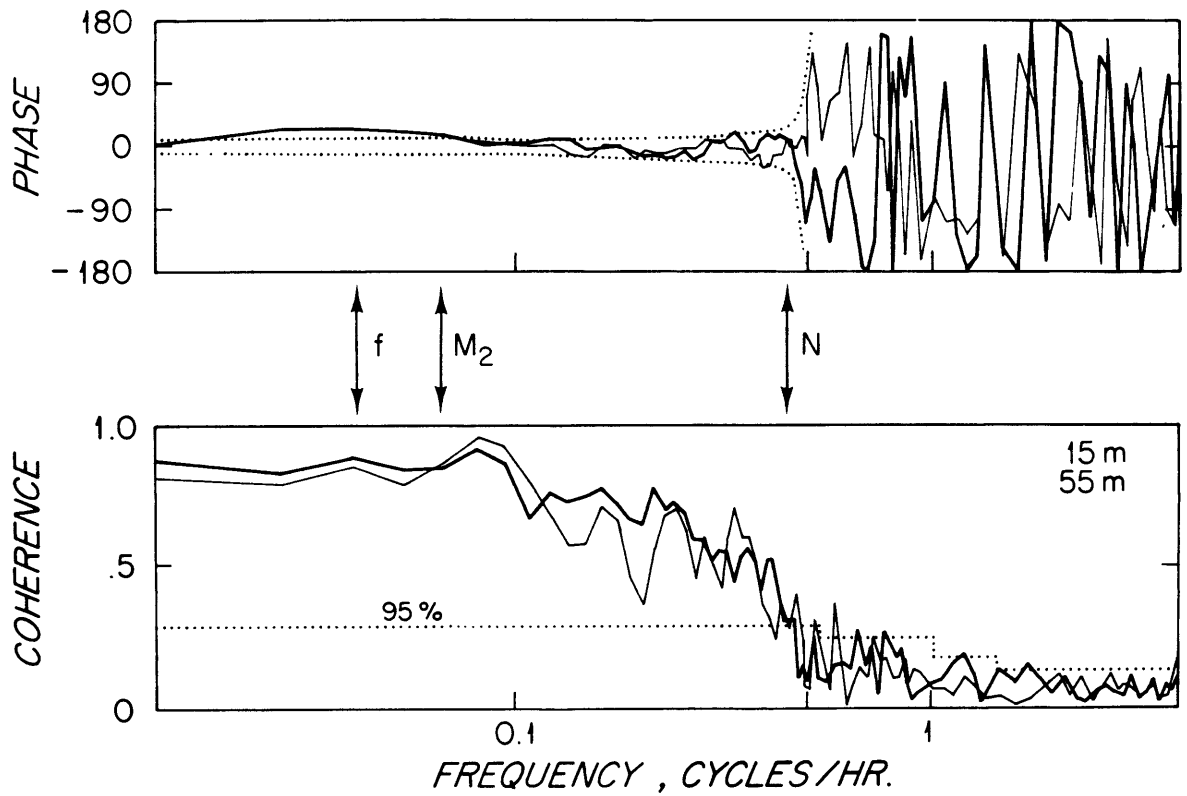
Figure 4

Cross spectra between east (heavy line) and north (light line) velocity
components of 15 m and 55 m instruments, computed as figure 1. The 95%
level of no significance and 95% confidence limits for zero phase are
shown as dotted lines (Koopmans, 1974). The 15 m level leads the 85 m
level at the inertial frequency.

approach, which will be employed here, is to filter the observed velocities to form the time series of velocity within a particular spectral band. The variations in this filtered velocity are then compared with the observed density structure, so that features of the velocity field which are correlated with the density structure may be identified. This technique has been applied to frequency bands spanning the superinertial range of frequencies shown in figure 2. Significant structure is found only for high frequency (> 1 cph) and near inertial bands, as might be expected from the mean spectra. The results for these two bands are discussed in the following two chapters.

Chapter 4. Observations of high frequency velocities

The benthic boundary layer is believed to be turbulent. An increasing level of high frequency velocity fluctuations is seen in this experiment near the bottom (figure 2). In this chapter these fluctuations are shown to be consistent with the expected energy level of boundary layer turbulence, and their intensity is correlated with the observed density and lower frequency velocity fields.

East and north velocities from each instrument were high pass filtered with an 11 element smooth non-recursive filter constructed by an algorithm described in Hamming (1977). The frequency response of this filter is shown in figure 2. Large spikes in the filtered signal are caused by instrument rotor stalls. These spikes have been eliminated in the processing. The velocity signals processed in this way will be called high pass velocity.

The velocity measured by the VACM sensors (rotor and vane) is vector averaged by the VACM electronics over a 7.5 minute interval. The recorded velocity is thus a low pass filtered version of the velocity measured by the sensors. The combination of this VACM low pass filter and the digital high pass filter described above yields a band pass filter with a maximum energy transmission of .6 and an equivalent 50 per cent energy transmission pass band from 2 to 5 cph. Assuming the VACM sensors to be perfect, the transfer function between the oceanic velocity and the computed high pass velocity is described by this band pass filter.

Observed high pass velocities

Figures 5, 6 and 7 display the high pass velocity signal for 3 periods. Various features of the observed high pass velocity are illustrated in these figures and are discussed below. The complete record of high pass energy is displayed in figure 8c. The corresponding potential temperature and 1 day mean speed records are shown in figures 8b and 8a.

A thick mixed layer: Figure 5a shows the high pass north velocity for each instrument. The amplitude of the high pass fluctuations is clearly modulated at slower time scales. Figure 5b displays contours of filtered high pass energy, as a function of time and height off the bottom. The energy time series are calculated from the high pass east and north velocity time series. These are then filtered with a half cosine filter of half width 3 hours to form the high pass energy time series displayed in figure 5b. The correspondence between regions of large high pass energy in figure 5b and large amplitude fluctuations in figure 5a should be clear.

Figure 5c shows 2 m°C isotherms of potential temperature as a function of time and height off the bottom. The potential temperature here, and in all subsequent figures, is filtered with a half cosine filter of half width 3 hours, the same filter used on the high pass energy in figure 5b. A 45 m thick, well defined bottom mixed layer is present from July 26 to August 1. The lower frequency velocity during this period is approximately the same at all levels and consists of a steady 7 cm/s current with approximately 1 cm/s internal wave fluctuations (figure 8a).

19

Figure 5

High pass velocity during a period of thick mixed layer

a)   High pass north velocity for all 7 instruments. Frequency response
      of high pass filter is shown in figure 2. Data from each instru-
      ment is plotted so that zero velocity corresponds to the height
      of that instrument off the bottom as shown on the left hand axis.
      The data at 75 m is formed by averaging the 65 m and 85 m data.

b)   Contours of filtered high pass energy, plotted as a function of
      time and height off the bottom on the same scale as a). The
      energy is formed from the individual high pass velocity components
      and then filtered with a half cosine filter of half width 3 hours.
      Notice how clouds of high pass energy intermittently fill the
      mixed layer shown in c).

c)   Contours of potential temperature filtered as in b) plotted on
      same scale.

d)   Least squares ellipses fit to successive 24 hour pieces of high
      pass velocity. The ellipses are rotated so that high pass
      velocity fluctuations parallel to the 24 hour mean velocity are
      horizontal on the figure; velocity fluctuations perpendicular to
      the 24 hour mean velocity are vertical. The size and orientation
      of these ellipses show the energy and directionality of the high
      pass velocity, respectively.

V' $\;I\;$ .2 cm/s   a

METERS ABOVE BOTTOM

$\langle U'^2 + V'^2 \rangle$ .004 cm^2/s^2 contours   b

V

θ .002 contours   c

METERS ABOVE BOTTOM

I 01 cm^2/s^2 d

23   25   27   29   31   2   4

JULY 77   *AUGUST 77*
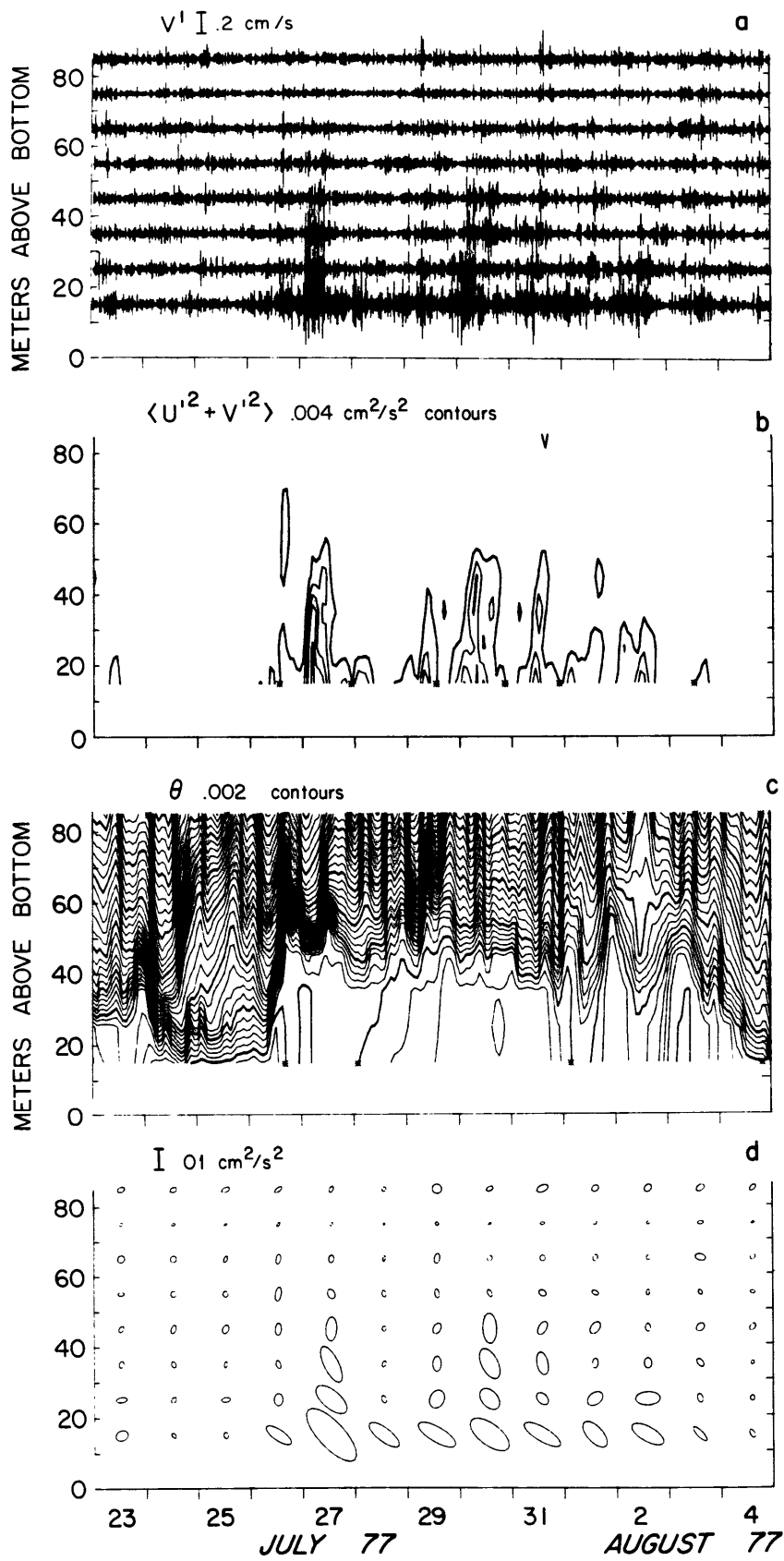
Comparing the high pass energy seen in figure 5b with the density struc-
ture shown in figure 5c reveals clouds of high pass energy extending from
the bottom and intermittently filling the mixed layer. This looks like
bottom generated turbulence. It is more intense near the bottom, and is
present only when the mixed layer is present. Below, the energy and
frequency of these fluctuations is shown to be similar to that expected
for bottom turbulence.

Strong density gradients: Figures 6b and 6c show high pass energy and
potential temperature contours as in figures 5b, c. The density struc-
ture is more complex here with a frontlike feature on June 4 and 5, a
shallow mixed layer from June 5 to 9 and a thick mixed layer starting on
June 9. Note that the potential temperature contour interval is 5 m°C
as opposed to the 2 m°C in figure 5. The density gradients above the
mixed layer are much stronger here than in figure 5. The mean speed is
also much lower during this period. Figure 6a marks times during which
the VACM rotor did not move. During these periods the calculated high
pass velocity is zero.

Figure 6b shows the high pass energy for this period. Intermittent
near bottom maxima of high pass energy, similar to those in figure 5b,
are seen here within the thick mixed layer starting on June 9. Here,
however, they are much less energetic, and do not extend to the mixed
layer top. Unlike in figure 5b, much of the high pass energy is here co-
herent with the regions of strong temperature gradient; the front on
June 4, 5 and the mixed layer cap starting on June 7 clearly correspond
with regions of large high pass energy. The high pass energy associated
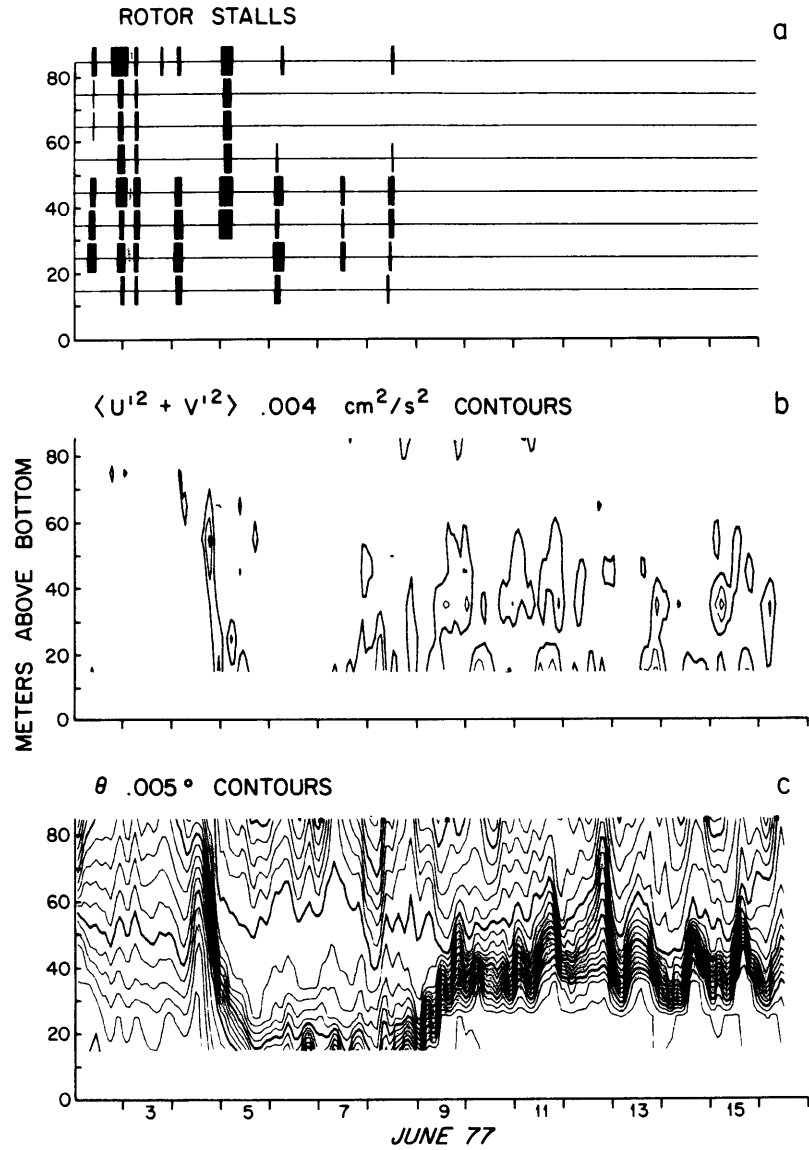
Figure 6

High pass velocity during a period of strong density gradients.

a) Regions of rotor stall for each instrument, plotted as in figure 5a
   Dark regions indicate a stall.

b) As figure 5b.

c) As figure 5c, but 5m°C contour interval.

23

with these temperature gradients is distinct from the near bottom, presumably turbulent, high pass energy. It may result from advection of small scale, low frequency shear, associated with the temperature gradients, by the low frequency horizontal current. Significantly, the interior homogeneous region extending from June 5 to 8, shows little high pass energy. If this is a detached bottom mixed layer, as hypothesized by Armi and D'Asaro (1980) it clearly does not show the same level of high pass energy as the bottom mixed layers. This suggests that it is no longer actively turbulent.

A complex region: Figure 7 shows the high pass energy and potential temperature structure during a third period, characterized by rapid changes in the mixed layer characteristics and a large (10 cm/s) mean current. During this period interior homogeneous layers merge with bottom mixed layers on 3 occasions: June 26, June 29 and July 2. Mixed layer detachment may be occurring here as hypothesized by Armi and D'Asaro (1980).

The high pass energy structure shows many features seen previously. The bottom intensified maxima on June 27, July 2, and July 3 appear similar to those in figure 5; the maxima on July 3 extends to the mixed layer top 50 m above the bottom. The region of strong temperature gradient from June 23 to June 26 is accompanied by regions of large high pass energy, as in figure 6. The numerous interior homogeneous layers show a generally low level of high pass energy. The maxima in high pass energy on June 26, however, occurs within a bottom mixed layer, which is continuous with an interior layer. This feature is unusual in that it

$\langle U'^2 + V'^2 \rangle$ .004 cm^2/s^2 CONTOURS a

θ .005 CONTOURS b

23   25   27   29   1   3

JUNE 77   JULY 77

METERS ABOVE BOTTOM
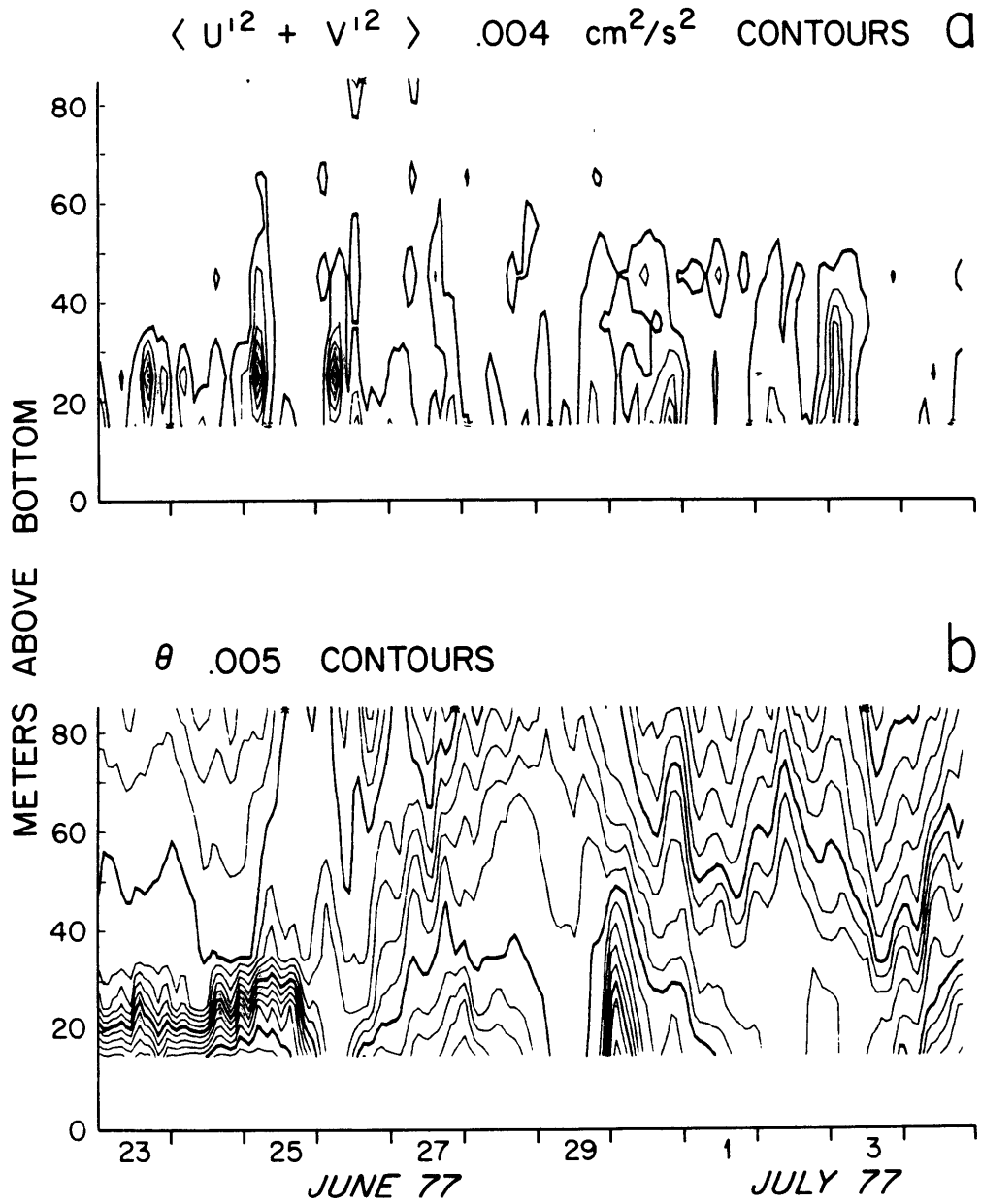
Figure 7

High pass velocity during a period of complex density structure.

a)   As figure 5b.

b)   As figure 6c.

25

Figure 8

Mean velocity, density, high pass velocity and near inertial velocity
structure for entire record. All figures plotted with same vertical
and horizontal scales. Differences in start and stop times are due to
differences in averaging.

a)   Left axis: 1 day mean speed at 15 m. Right axis: Turbulent
      Ekman layer height, $.4u*/f$, computed using $u* = S/30$.
      S is 1 day mean speed.

b)   Potential temperature contours as in figure 6c.

c)   High pass energy contours as in figure 5b.

d)   High pass velocity ellipses as in figure 5d.

e)   Contours of near inertial clockwise energy computed as described
      in the text. The spectral response of the near inertial filter
      is shown in figure 2. A nearly independent estimate is computed
      every 60 hours.

f)   Contours of near inertial phase of each instrument relative to
      the phase of the vertical mean near inertial velocity. Clockwise
      leading phases are shaded. Phase contours are not shown when
      near inertial energy is less than $.25 \ cm^2/s^2$.

1 DAY MEAN SPEED (cm/s)

TURBULENT
EKMAN LAYER
HEIGHT (m)

a

POTENTIAL TEMPERATURE contour interval 005° C

b

HIGH PASS ENERGY contour interval = 006 cm²/s²

c

HIGH PASS ELLIPSES ⊥ 01 cm²/s² downstream

d

INERTIAL ENERGY contour interval = 5 cm²/s²

e

INERTIAL PHASE contour interval = 5°

f

MAY 1977   JUNE   JULY   AUGUST

27
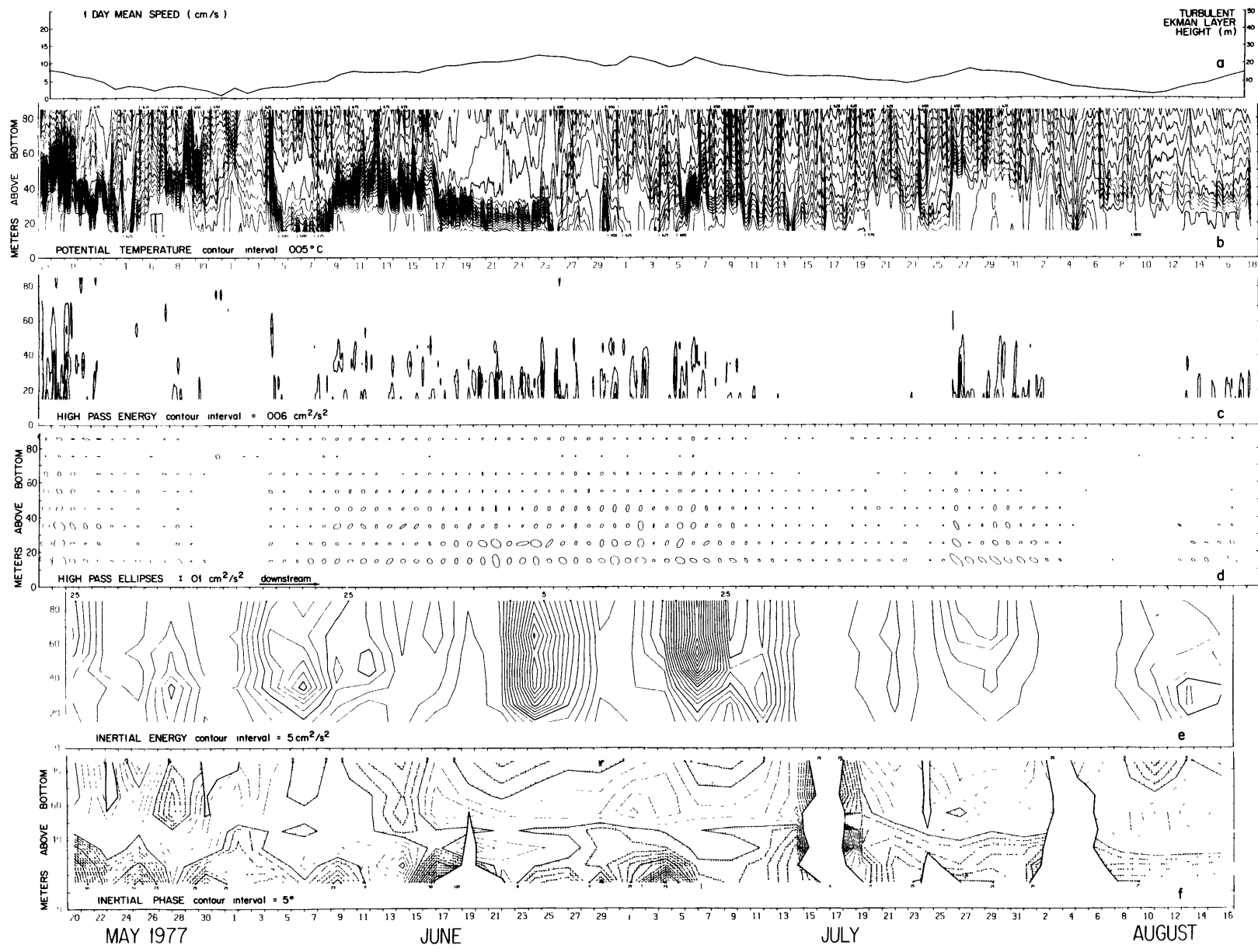
is not bottom intensified, but occurs within a well mixed region. A separated turbulent boundary layer would have such a mid-water maximum in turbulent kinetic energy.

Expected Turbulence Properties

The above observations reveal two major kinds of high pass velocity fluctuations, fluctuations occurring within regions of strong temperature gradient, and bottom intensified fluctuations occurring within the bottom mixed layer. This second variety of fluctuations looks like bottom generated turbulence. In this section the expected properties of such bottom generated turbulence are defined and a comparison with the observed properties is made.

The turbulence in the benthic boundary layer is probably generated by a mechanism similar to that operating in a two dimensional laboratory turbulent boundary layer, such as can be produced in a wind tunnel or flume. Such boundary layers have been extensively studied and their properties are well known. The extrapolation of these measurements to the benthic boundary layer will define the expected properties of the boundary layer turbulence.

Friction velocity: The turbulent velocity fluctuations within the boundary layer are expected to scale with $u*$, the friction velocity, where $\rho u*^2$ equals the wall drag. Since $u*$ is not measured in this experiment it must be estimated from the measured velocity at 15 m. The important parameters in this estimate are the bottom roughness and the Reynold's number, $Re = U_1 \delta / \nu$. An interior velocity $U_1 = 10$ cm/s and

a boundary layer height of $\delta = 20$ m yield $Re = 2 \times 10^6$. For a smooth wall turbulent boundary layer at this Re, a value of $U_1/u^* = 35$ is predicted using the Millikan drag law (Millikan, 1939). Bottom photographs of the Hatteras Abyssal Plain show a flat bottom with occasional 1 cm bumps (Biscaye and Eittreim, 1977). A sand grain roughness of $\ell = 1$ cm, which certainly overestimates the effect of these bumps, yields a roughness Reynold's number $u^*\ell/\nu$ of approximately 30, which is transitional between smooth and rough flow (Hinze, 1959, p. 486) and predicts $U_1/u^* \sim 29$. Csanady's (1967) Ekman drag formula with $z_o = \nu/u^*$ yields $U_1/u^* = 34$. A value of $U_1/u^* = 32$ will be used below.

Frequency and energy: Figure 9a shows the measured turbulent velocity fluctuation intensity through a laboratory turbulent boundary layer (Klebanoff, 1954). The turbulent velocity fluctuations scale with u^* and become small above δ_{99}, the boundary layer thickness. In the outer part of the boundary layer the horizontal kinetic energy due to these turbulent velocity fluctuations is approximately u^{*2}. Using $U_1/u^* = 32$, this yields $u^{*2} = 10^{-3} U_1^2$.

The high pass energy is sensitive only to velocity fluctuations within a particular range of frequencies. Do the expected turbulent velocity fluctuations have energy in this frequency range? Figure 9b shows the spectra of downstream and crossstream velocity fluctuations in the outer part of a laboratory turbulent boundary layer (Bradshaw, 1966). Velocity spectra in the outer part of a laboratory turbulent
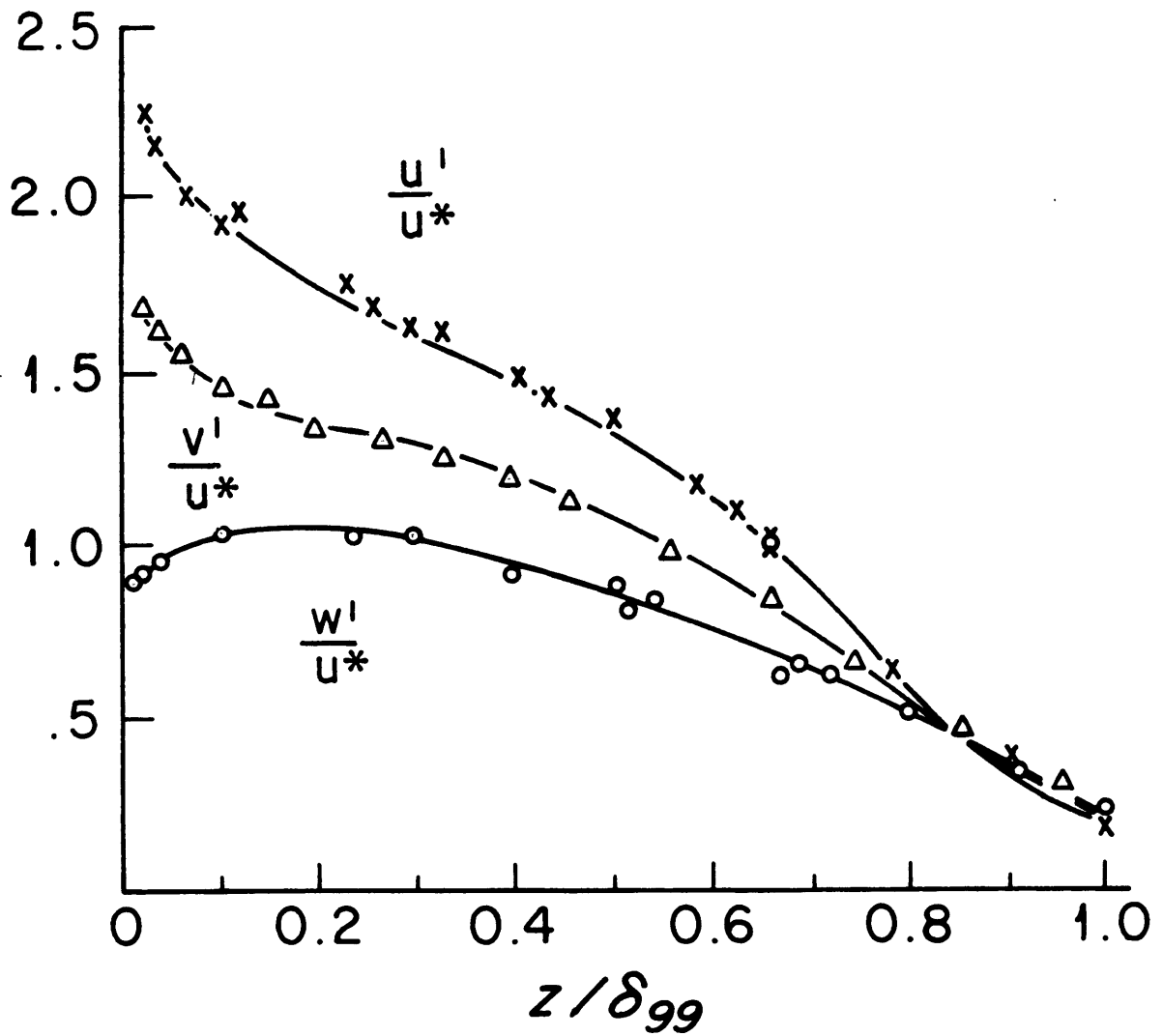
Figure 9a

Turbulent velocity fluctuations through a laboratory two dimensional
turbulent boundary layer (from Hinze, 1959, pg. 488). z/δ_{99} is frac-
tional height within the boundary layer.

Figure 9b

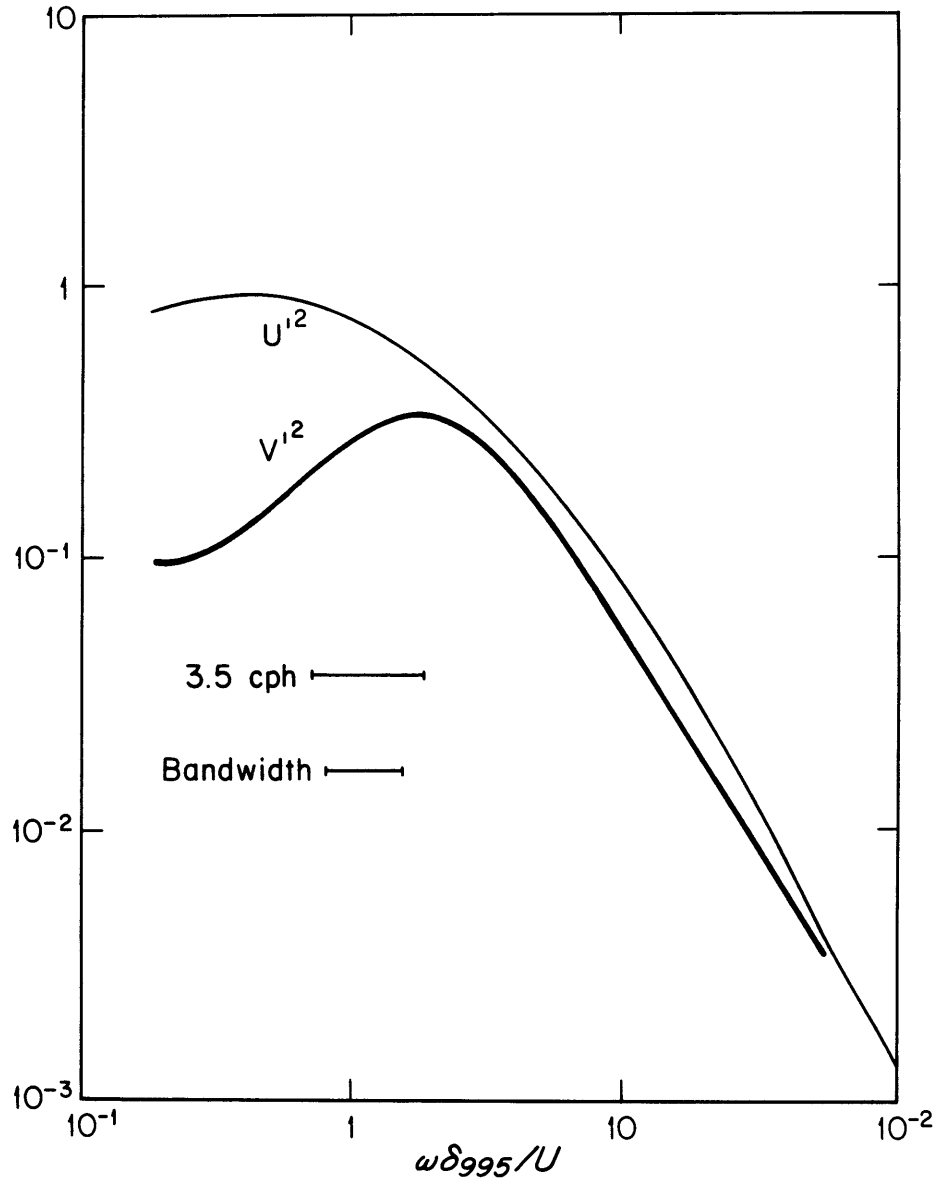Spectrum of turbulent velocity fluctuations in a laboratory two dimen-
sional turbulent boundary layer (Bradshaw, 1966). z/δ_{995} = .89.
Vertical axis is arbitrary. Center frequency of high pass filter is
shown in same nondimensional coordinates for a range of U (5-10 cm/s)
and δ_{995} (10-20 m). The half power bandwidth of this filter is also
shown.

31

Ekman layer are similar (Caldwell et al. 1972). Plotted in the same

non-dimensional coordinates is the high pass energy central frequency,

3.5 cph, for a range of mean speeds, 5-10 cm/s, and a range of δ_{995},

10-20 m. The high pass energy central frequency is seen to be near the

spectral peak of the expected turbulent velocity fluctuations. The high

pass energy should thus be an excellent indicator of the presence of

turbulent boundary layer velocity fluctuations.

The half power bandwidth of the high pass velocity transfer func-

tion is also shown in figure 9b. Roughly 20 per cent of the turbulent

horizontal kinetic energy shown in figure 9b is contained within this

bandwidth. Since this is a 50 per cent transmission bandwidth a

measurement of high pass energy in the outer part of a turbulent boun-

dary is expected to yield approximately 10 per cent of the total tur-

bulent horizontal kinetic energy or $(.01 \ U_1)^2$.

Stratification: The mixed layers observed in this experiment commonly

show a slightly stable density stratification, measured by potential tem-

perature. Stable density stratification can strongly influence a tur-

bulent boundary layer and if sufficiently strong can suppress the tur-

bulence completely (Turner, 1973; Arya, 1972). Assuming the energetic

eddies in the outer part of the boundary layer to be of the same scale

as the boundary layer, H = 10 m and that they have an energy density

$u*^2$, U_1 = 7 cm/s gives a kinetic energy of $u*^2 \ H \sim 48 \ \text{ergs/cm}^2$.

Assuming that these eddies will completely mix any existing stratifica-

tion $\Delta\rho$ on the scale H, this will require energy $g\dfrac{\Delta\rho}{\rho}\dfrac{H^2}{12}$. Using

$g \ \dfrac{\Delta\rho}{\rho} = .1 \ \Delta\theta$ and H = 10 m, 4 ergs/cm^2 are required to mix a tem-

perature gradient of .5 m°C/10 m, typical of a mixed layer, while 80 ergs/cm^2 are required to mix the typical 10 m°C/10 m temperature gradient above the mixed layer. Thus the typical stratification within the mixed layer can be mixed by the boundary layer turbulence without suppressing this turbulence. Boundary layer turbulence in the strati-fied fluid above the mixed layer, however, will be strongly damped by the stratification. Velocity fluctuations in the stratified region are thus likely to be wavelike, rather than turbulent (Csanady, 1978; Turner, 1973; Piat and Hopfinger, 1980). Boundary layer turbulence is therefore expected only within the bottom mixed layer.

Is it turbulence?

Figure 10 shows scatter plots of (high pass energy)$^{1/2}$ versus speed at 85 m (10a) and 15 m (10b) for the entire 92 day record. Speed is here formed from the east and north velocity components filtered with a half cosine filter of 3 hour half width. The 15 m instrument is commonly in a mixed layer, while the 85 m instrument never is. At 85 m the high pass energy displays a constant level of approximately (.04 cm/s)^2 inde-pendent of speed except at low speeds where the finite threshold of the VACM is important. At 15 m the fluctuation intensity is much higher, approximately .1 cm/s at a speed of 10 cm/s and is roughly correlated with speed. At 15 m the high pass energy level is consistent with the expected properties of boundary layer turbulence, i.e., the velocity fluctuations scale with speed, and have a magnitude of .01U. This is not true at 85 m.
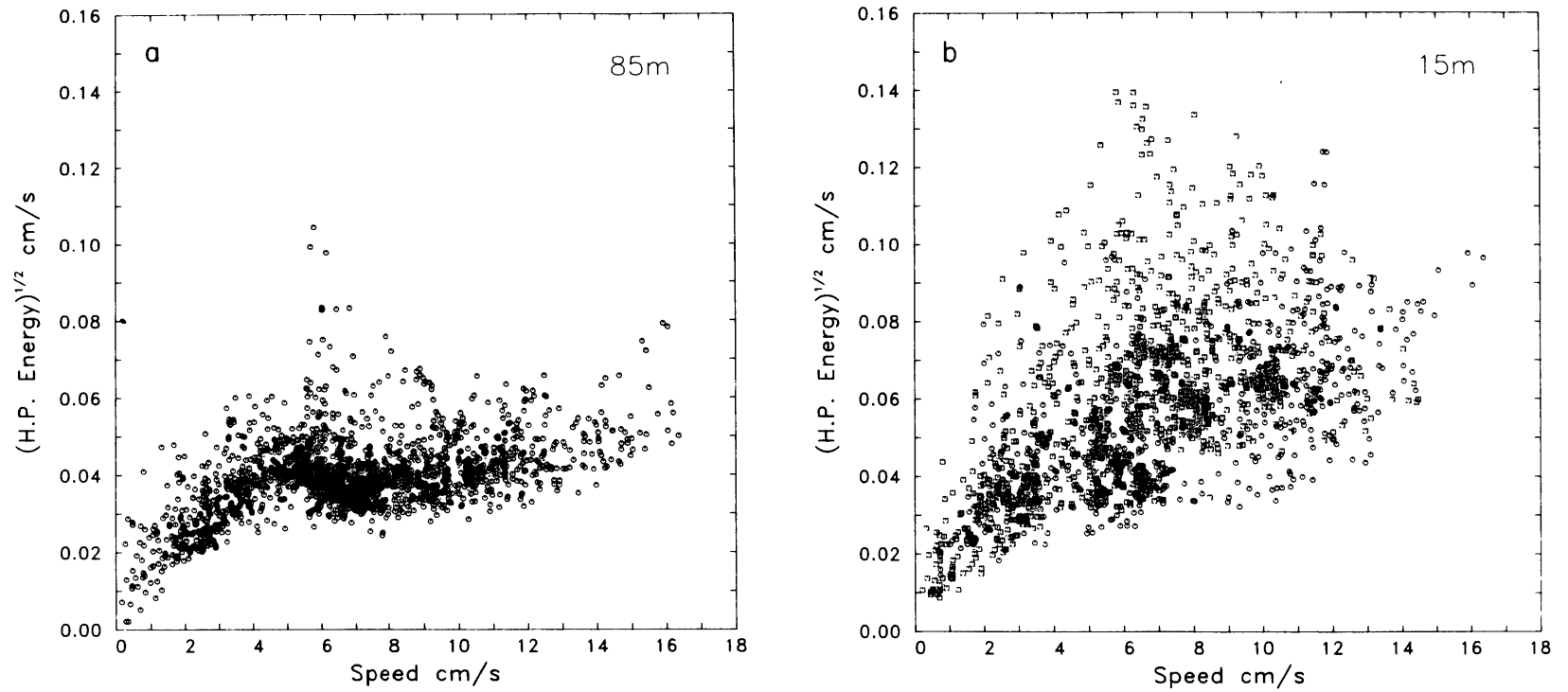
Figure 10

Scatter plot of (3 hour half width, half cosine filtered high pass energy)$^{\frac{1}{2}}$ versus $(\overline{U} + \overline{V})^{\frac{1}{2}}$ with $\overline{U}$ and $\overline{V}$ 3 hour half width, half cosine filtered east and north velocities.

a) 85 m instrument; this instrument is never in a mixed layer.

b) 15 m instrument; this instrument is commonly within mixed layers.

The observed high pass velocity fluctuations appear to be due primarily to boundary layer turbulence. This is supported by the following observations: The high pass velocity is sensitive to velocity fluctuations near the expected spectral peak of boundary layer turbulence (figure 9b). The observed high pass energy level is roughly correlated with the lower frequency velocity (figure 10b) as expected for boundary layer turbulence; the high pass energy level is consistent with the expected turbulent energy level. Boundary layer turbulence should be confined to the mixed layer, and be more energetic near the ocean bottom. The high pass energy in figure 5 is certainly of this character, as is much of the high pass energy in figures 6 and 7.

Sources of high frequency velocity fluctuations other than boundary layer turbulence are also apparent in the data. The velocity fluctuations associated with the large temperature gradients in figures 6 and 7 are one example. The background level of high pass energy in figure 10a suggests an instrumental noise source. Simulations of VACM round off errors (McCullough, 1975) yield an intrinsic high pass velocity noise level of about .03 cm/s. This is comparable to the background energy level in figure 10a. Other instrumental sources of high pass energy, from mooring motion or imperfect sensor response, are possible. These sources, however, should be sensitive only to the velocity field, not to the boundary layer density structure. The observed fluctuations show a clear correlation with the boundary layer density structure. The high pass velocity, especially that part occurring with-

in bottom mixed layers, will thus be interpreted as due primarily to boundary layer turbulence.

The high pass velocity is a measure of boundary layer turbulence. Unfortunately, it is a quite limited one. It is sensitive only to velocity fluctuations in a narrow frequency range, which is estimated to contain only 10% of the total turbulent kinetic energy. Changes in either the frequency or energy of the turbulent velocity fluctuations will result in a change in the high pass energy, so that changes in high pass energy do not necessarily correspond to changes in the turbulent energy. The high pass velocity is also a noisy measure of boundary layer turbulence with a significant high pass signal coming from other oceanic velocity fluctuations (figure 6) and instrumental noise. The high pass velocity can therefore not be used to detail the structure of boundary layer turbulence, but only to indicate its approximate strength as a function of time. The measurements are further limited by the VACM locations to between 15 and 85 m above the bottom. Weatherly's (1972) observations of the boundary layer with a similar mean speed indicate that this is significantly above the logarithmic region of the boundary layer. Remembering all of the above limitations, the measurements of high pass energy provide a useful measure of the turbulence structure across the mixed layer, which can be compared with other measurements and theoretical constructs.

Observations of boundary layer turbulence

The high pass velocity shows several interesting aspects of the boundary layer turbulence. The turbulence appears to intermittently fill the entire bottom mixed layer. This is seen clearly in figure 5, starting on July 26; in figure 7 on July 3, and in figure 8 on May 18-21, May 30, July 11, and August 13-18. In figure 8a the turbulent Ekman layer height δ_{EK} = .4u*/f is plotted with u* = S/30, S being the speed computed from the 1 day mean velocity at 15 m. δ_{EK} is generally less than 15 m and usually is less than the mixed layer height (Armi and Millard, 1976). For example in figure 5 $\delta_{EK} \sim$ 15 m, while the mixed layer height and the penetration height of the boundary layer turbulence is approximately 40 m. Other examples can be seen in figure 7 on July 3 and in figure 8 on May 18-21 and August 13-18, while a counter example can be seen in figure 6 starting on June 9. These observations indicate that the boundary layer turbulence commonly extends above a turbulent Ekman layer height, in contrast to the expected properties of a turbulent Ekman layer. These observations are consistent with previous observations of Radon-222 (Sarmiento, 1978) in this area, which indicate that turbulent mixing, on the time scale of a few days, penetrates to the top of the mixed layer, and above a turbulent Ekman layer height.

Figures 5d and 8d display the directionality of the high pass horizontal velocity. For each 24 hour period the best least squares ellipse is fit to the two components of high pass velocity (Calman, 1978). These ellipses are plotted for each day and rotated so that a vertical line

corresponds to high pass velocity fluctuations oriented perpendicular to the 24 hour mean velocity, while a horizontal line corresponds to fluctuations oriented parallel to the 24 hour mean velocity. Figure 5d clearly shows a concentration of high pass energy within the mixed layer and near the bottom. The velocity fluctuations are seen to align themselves roughly 45° clockwise of the mean velocity whenever the bottommost instrument is within a mixed layer. A preference for this general direction can also be seen in figure 8d (May 18-21, May 28, July 5-10, August 12-16). Assuming that these turbulent fluctuations are generated by the lower frequency mean velocity, this asymmetry between the direction of the mean velocity and the orientation of the fluctuations, suggests that rotation, which enters the equations of motion in an asymmetrical way, must be important in the dynamics of the boundary layer.

The discussion of these observations is postponed to chapter 6, so that the observations of the near inertial motions, which yield additional information on the boundary layer turbulence, may be described.

Chapter 5. Observations of near inertial velocities

The average horizontal kinetic energy spectra shown in figure 2

indicate less near inertial energy in the bottommost instruments than

in the upper instruments. Similar near bottom decreases in near inertial

energy have been observed by Kundu (1976), Hayes (1980) and Leaman (1976)

and can clearly be seen in figure 5 of Weatherly and Wimbush (1980). In

the following section the relation of this decrease to the bottom mixed

layer structure is examined.

The 92 day velocity record from each instrument was broken into 36,

120 hour long 50% overlapping pieces. The near inertial clockwise and

anticlockwise components of velocity in each piece were found using a

demodulation filter with center frequency of 1/24 cph and a 4-term

Blackman-Harris window described by Harris (1978). The spectral re-

sponse of this window is shown in figure 2. Near the center frequency

it has a shape similar to that of a Hanning window with a 72 hour piece.

The side lobes, however, are much lower. Several other windows have

been used and none of the results shown below depend critically on the

particular window used.

<u>Clockwise velocities</u>

Most of the near inertial energy is in clockwise motions (figure 3).

The analysis of the near inertial velocity will thus concentrate on the

clockwise component of motion. Figure 8e shows contours of clockwise

inertial energy as a function of time and height off the bottom. The

near inertial energy level is vertically coherent, but varies signifi-

cantly with time. There is clearly less near inertial energy near the
ocean bottom, as is seen in the average spectra (figure 2). The height
at which the energy decreases most rapidly, however, varies with time.
Comparing 8e with the 5 m°C isotherms of potential temperature displayed
in figure 8b, the height at which the inertial energy decreases most
rapidly is seen to correlate with the height of the bottom mixed layer.
For example, both the mixed layer height and the height of maximum
gradient are large on May 20 and July 27-31. On June 21-29 and August
12-16 they both are small. The mixed layer top and the height of max-
imum gradient both decrease 20 m between July 6 and July 13. The major
exception to this pattern occurs on May 28, when a maximum in inertial
energy is seen at the mixed layer top. At this time, however, the mean
velocity is small (figure 8a) and any turbulent boundary layer effects
will thus be small. In general the mixed layer exhibits less near
inertial energy than the interior, with the maximum gradient in energy
occurring slightly above the top of the mixed layer.

Figure 8f shows contours of the phase of the clockwise inertial
velocity at each level relative to the phase of the mean clockwise
inertial velocity. Using the vertical mean as a reference rather than
a particular level allows all levels to be treated identically. Regions
of negative phase lead the mean and are shaded. The computed phases
are not shown when the near inertial energy is less than .25 cm^2/s^2;
they are quite noisy at these times.

The computed phases clearly show the 15 m instrument leading, on the average, relative to the mean, and leading almost always relative to the 25 m instrument. The typical phase difference of 25° is significantly larger than any expected instrumental errors. Unlike the energy, the near inertial phase exhibits large gradients within the bottom mixed layer, for example on May 20-26, June 3, July 3 and August 10-15. Similar gradients do not generally appear above the mixed layer.

The phases computed here clearly show the apparent instrumental direction errors discussed in chapter 2. Instruments 2 and 3 show a consistently positive (anticlockwise) phase, while instruments 1 and 4 show a consistently negative (clockwise) phase. This effect is especially striking in late June and early July in the long tongues of negative phase at 45 m (instrument 4).

The phase structure of the near inertial motions shows far less correlation with the density structure than does the energy. Although this may reflect the physics of the boundary layer it may also be due to the much higher noise level in the phase measurement. Spectral leakage from adjacent frequency bands affects phase more strongly than energy since these other frequencies, by definition, have rapidly varying phase with respect to the inertial frequency. The spectral leakage is also more severe for phase, being proportional to the filter transmission, rather than the transmission squared as for energy. Finally the phase, unlike horizontal kinetic energy, is sensitive to instrumental direction errors.

Anticlockwise velocities

The near inertial anticlockwise motions are much less energetic than the clockwise motions. They do not show the strong correlation with density structure found for the clockwise motions; energy and phase diagrams similar to figures 8e, f are therefore not shown here.

Simple WKB internal wave theory predicts a ratio Γ of clockwise to anticlockwise energy of $\Gamma = (\sigma + f)^2/(\sigma - f)^2$ for $\sigma \sim f$ (Fofonoff, 1969). Fu (1980), accounting for the variability of f with latitude, finds this prediction should be valid for $\sigma > 1.01f$. The value of Γ observed here is not consistent with these predictions. For example, figure 2 shows, $\Gamma = 50$, at $\sigma = f$, corresponding to a WKB prediction of $\sigma = 1.33f$. There is more anticlockwise energy than is predicted. This suggests that much of the observed anticlockwise motion is not due to internal waves. Fu (1980) finds a similar excess of near inertial anticlockwise energy in a large number of North Atlantic current meter measurements.

Anisotropy

The directionality of the near inertial motions can be examined by computing the average variance ellipse. Following Gonella (1972) and Calman (1978) the amplitude and phase of

$$R = \frac{\hat{C}(\sigma) \; \hat{C}(-\sigma)}{|\hat{C}(\sigma)| \, |\hat{C}(-\sigma)|}$$

defines the stability and direction of the average ellipse. $C(\sigma)$ and $C(-\sigma)$ are the clockwise and anticlockwise amplitudes for the near

inertial band. The ellipse stability has the same form and probability distribution as a coherence; if it is significantly different from zero, the ellipse is significantly anisotropic.

Table 1 lists the ellipse properties computed for the top instrument using the same Fourier transforming procedure used to make figure 8e, f. These ellipse parameters are computed in both an east/north (geographical) coordinate system, and with each Fourier transformed piece rotated so that the central one day mean velocities in each piece are parallel (velocity coordinate system). The one day mean velocity points roughly east for most of the record. The near inertial velocities show a small but significant anisotropy, in either coordinate system, with the major axis of the ellipse pointing in the direction of the mean velocity. The anisotropy is somewhat stronger in the velocity coordinate system.

If the observed velocity fluctuations are interpreted as internal waves, the direction of the velocity ellipse gives the direction of wave propagation (Calman, 1978). Here, this would indicate waves propagating primarily parallel to 1 day mean velocity vector. This interpretation assumes, however, that the observed anticlockwise motions are due to internal waves, which, as discussed above, may not be true.

Table 1

Average Near Inertial Ellipse

	Geographical Coordinates	Velocity Coordinates
Major Axis (cm/s)	.93	.95
Minor Axis (cm/s)	.75	.73
Direction of Major Axis	7° from East	-3° from downstream
Ellipse Stability	.36	.43
95% level of no significance @ 72 EDOF	.29	.29

Summary

Motions in the inertial-gravity wave frequency band show a strong
boundary layer signal only near the inertial frequency. The near inertial
clockwise behavior is summarized in figure 11. Each arrow represents the
amplitude and phase of the near inertial clockwise velocity. The energy
decreases near the top of the mixed layer with little phase change.
Within the mixed layer the phase begins to lead, with the phase angle
increasing downward. Extrapolating to the bottom, the energy should
drop to zero, with an unknown phase. These variations may occur sig-
nificantly above a turbulent Ekman layer height.

The observed near inertial anticlockwise velocities do not show
a similarly simple pattern and contain more energy than is predicted by
simple internal wave theory. The near inertial motions are slightly
anisotropic with the major axis of the mean variance ellipse oriented
parallel with the 1 day mean velocity.
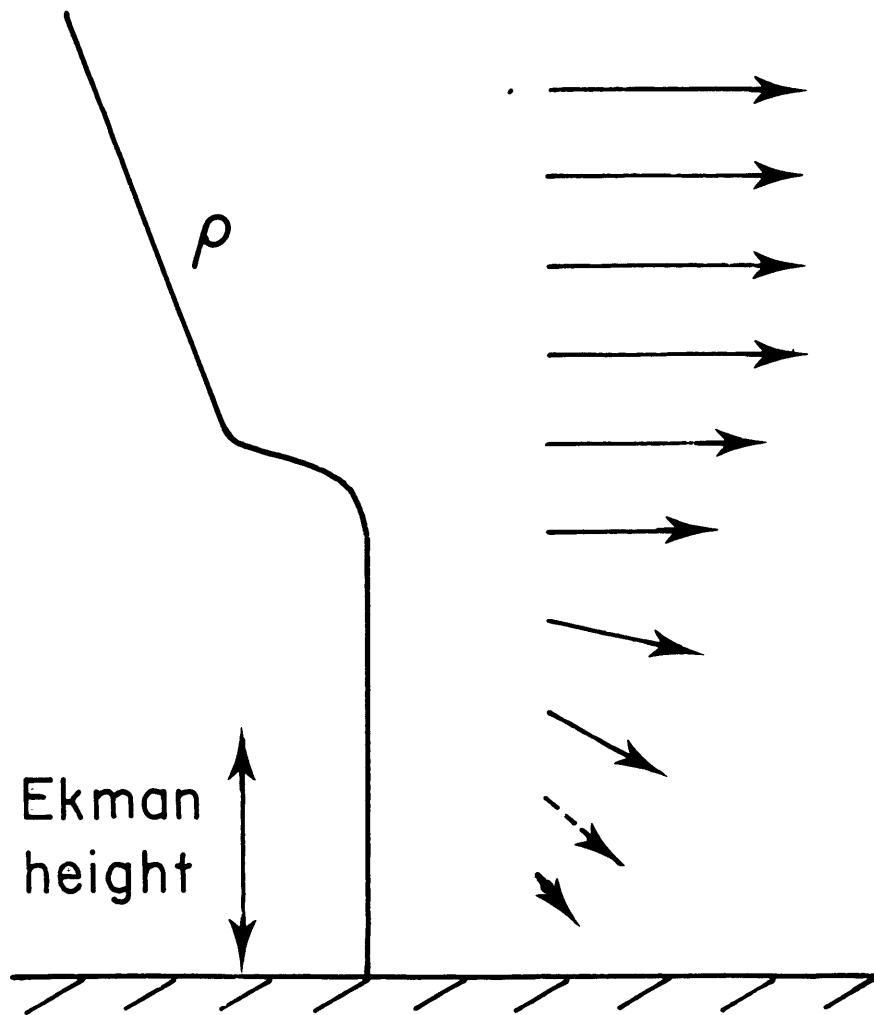
Figure 11

Summary of observed near inertial clockwise response. Arrows represent energy and phase of near inertial clockwise velocity. Near inertial energy decreases into the mixed layer, with the phase constant. Within the mixed layer the energy decreases slowly and the phase begins to lead the interior. The mixed layers are typically larger than a turbulent Ekman layer height.

46

Chapter 6. Discussion

    In chapter 7 the observed near inertial structure is interpreted
in terms of the interaction of the internal wave field with the boun-
dary layer turbulence. Here, the qualitative features of the observed
high pass and inertial structure are discussed.

    One possible model of the benthic boundary layer is a steady
turbulent boundary layer, entraining upward into the prexisting strati-
fication. If horizontal effects are small a one dimensional model
results, which is the benthic boundary layer analogue of one dimensional
upper ocean models (Garwood, 1979). Such models have been used to
model the benthic boundary layer (Weatherly and Martin, 1978; Csanady,
1974; Armi, 1977). Armi and D'Asaro (1980) find that the observed
density fluctuations in this area are due primarily to horizontal ad-
vection. This cannot be modeled using a one dimensional model.
Here, another problem with this class of models is seen. Three indi-
cators of boundary layer turbulence, the high pass velocity, the
near inertial velocity deficit, and the Radon-222 measurements
(Sarmiento, 1978), all indicate that the turbulence commonly extends to
the mixed layer top. Since the mixed layers are commonly thicker than
a turbulent Ekman layer, these observations indicate that the boundary
layer turbulence commonly extends above a turbulent Ekman layer height.
The very height of the mixed layer is also an indicator of the turbulence
penetration height (Armi and Millard, 1976).

The one dimensional steady boundary layer models used to model the benthic boundary layer should become identical to the turbulent Ekman layer model in the limit of no stratification. In particular the predicted thickness should become the turbulent Ekman layer height in this limit. The presence of stratification should decrease the predicted boundary layer height (Businger and Arya, 1974). The observations here, therefore, show a boundary layer much thicker than would be predicted by steady, one dimensional models.

A striking feature of the high pass energy shown in figure 5 is the highly intermittent character of the boundary layer turbulence. At times the turbulence extends throughout the mixed layer, while a few hours later it is completely absent. These variations occur on tidal and inertial time scales. This suggests that the observed fluctuations in the boundary layer may be driven by the oceanic internal wave field, which has similar time scales.

A laminar Ekman layer, when subject to a clockwise rotating interior flow of frequency σ, increases in height by the factor $\left|1 - \sigma/f\right|^{-\frac{1}{2}}$ leading to an infinite height for inertial forcing (Greenspan, 1968). Figure 3 shows that near inertial clockwise motions are present in a significant amplitude. This suggests that they may thicken the boundary layer. Weatherly et al. (1980) using a turbulence closure model to simulate the boundary layer in this region find that the addition of inertial forcing results in a doubling of the boundary layer height. This mechanism may explain the thickness of

48

the observed boundary layer. It does not address the question of inter-
mittency.

Turbulent boundary layers are known to be quite sensitive to the
acceleration or deceleration of their driving flow. For two-dimensional
boundary layers deceleration results in a decreased drag coefficient, a
more rapid growth rate, higher turbulence levels, and if continued suf-
ficiently long, separation (Yaglom, 1979; Goldstein, 1965). It seems
plausible, therefore, that the observed intermittency in the benthic
boundary layer, is driven by the intermittent internal wave deceleration
of the boundary layer. Application of a simple scaling theory (D'Asaro,
1980) to the benthic boundary layer predicts that the observed internal
wave decelerations should lead to a significant increase in boundary
layer thickness on a few hours time scale. The data, however, indicate
no significant correlation between high pass energy at 15 m and the de-
celeration of the 15 m velocity in either a downstream or crossstream
direction. A correlation between the internal wave vertical velocity
and boundary layer thickness might also be expected. Using the 85 m
temperature variations to compute the vertical velocity, no correlation
is found. Thus although the observed boundary layer fluctuations may
be driven by the internal wave field, no direct evidence of this is
found.

The possibility remains that the observed boundary layer height
and intermittency are not due to the unsteadiness of the interior
velocity, but is instead an intrinsic feature of the benthic boundary
layer driven by a steady velocity. "Bursting" intermittency, with a

period of roughly 2.5 δ/U is commonly observed in the outer part of tur-
bulent boundary layers (Kovasznay et al., 1970; Falco, 1977) where δ
is the thickness of the boundary layer. Using $\delta = 20$ m, $U = 7$ cm/s,
a "bursting" period of less than an hour is expected. This is much
shorter than the observed intermittency period. The observed intermit-
tency is thus probably not due to "bursting".

A laminar Ekman layer is unstable at sufficiently high Reynold's
number. Could the boundary layer fluctuations observed here be due to
a similar type of secondary circulation within the turbulent Ekman layer,
as postulated by Brown (1970)? The calculated instabilities for a lami-
nar Ekman layer (Lilly, 1966; Faller and Kaylor, 1966) have a frequency
of magnitude much larger than f(e.g., Caldwell and van Atta, 1970,
fig. 16) which changes sign very near the fastest growing instability.
Thus the predicted frequency of the fastest growing wave, is highly
variable depending on exactly which wave is chosen. Most likely, how-
ever, the frequency is much larger than f, and thus cannot account
for the boundary layer variations observed here. It should be noted
that Caldwell and van Atta (1970) and Deardorff(1970) see no evidence
of laminar Ekman layer instabilities at the high Reynold's numbers
characteristic of the turbulent Ekman layer.

In summary then, no satisfactory explantion for the origin of
the clouds of turbulence seen in figure 5 has been found. The obser-
vations are not consistent with a steady, turbulent Ekman layer, as far

50

as its properties are known. Although internal wave forcing may cause the boundary layer to become thicker than a turbulent Ekman layer height, no correlation between the observed turbulence fluctuations and observed internal wave fluctuations is found.

The observed high pass and near inertial velocities both show a distinct mixed layer signal which is here attributed to boundary layer turbulence within the mixed layer. Careful examination of the calculated high pass and inertial velocities reveals, however, that the mixed layer signal for both extends some distance into the stratified fluid. This suggests that the boundary layer velocity fluctuations and stresses extend into the stratification, perhaps partially as evanescent fluctuations (Phillips, 1955) or high frequency, stress carrying, internal waves (Csanady, 1978). This may be important in the entrainment of fluid into the mixed layer. The boundary layer model of Weatherly and Martin (1978) exhibits a similar behavior, with the computed turbulence intensity and the diffusion coefficients diminishing to zero only above the mixed layer top.

Chapter 7. Internal wave interaction with the boundary layer

During the last decade great progress has been made in describing the space-time structure of the internal wave field (Garrett and Munk, 1979; Gregg and Briscoe, 1979). Still elusive, however, is a clear understanding of the dynamics of the internal wave field and the magnitude and character of its sources and sinks. One possible location of internal wave generation and/or absorption is the benthic boundary layer. The boundary layer is known to have characteristics distinct from the oceanic interior (Bowden, 1978), and is certainly the site of considerable energy dissipation. How much of this dissipated energy comes from the internal wave field? Leaman (1976) estimates a net downward energy flux in the internal wave field of .2 - .3 ergs/cm^2/s for a 4 day period in the Sargasso Sea. Müller et al. (1978), analyzing the IWEX experiment, find a similar asymmetry confined to the near inertial frequency band. Kundu (1976) finds a somewhat larger net downward flux in the near inertial band on the Oregon shelf. One interpretation is that this net downward energy flux results from absorption of near inertial waves by the benthic boundary layer. Fu (1980), however, proposes an alternative explanation based on the kinematic properties of surface generated near inertial waves. Below a direct estimate of the absorption of near inertial waves by the benthic boundary layer on a flat abyssal plain in the western North Atlantic is made.

Theoretical approach

The near inertial observations in chapter 5 indicate a signifi-
cant interaction between the near inertial motions and the boundary
layer. In the analysis presented below, these motions will be analyzed
as linear internal waves. The long non-linear interaction times com-
puted for the energy containing near inertial waves (McComas, 1977)
justifies this approach. McComas' calculations are based on thermo-
cline wave scales. In the deep ocean the wave scales are significantly
larger, and the non-linear interactions much weaker.

Consider a set of linear internal waves incident on a flat bot-
tomed ocean, with a thin turbulent bottom boundary layer. These waves
are superimposed on currents with much slower time scales here called
"mean" currents. In the absence of any waves the mean shear within the
boundary layer is balanced by the turbulent stress divergence. The
energy to maintain the stresses is drawn from the kinetic energy of the
mean flow. Any wave superimposed on this balance will modulate the
stresses. The energy to maintain the stresses may now come partially
from the wave as well as from the mean flow. If there are many waves,
the energy may be drawn from some unknown combination of these waves
and the mean flow. Since the boundary layer is highly non-linear one
should not expect the energy extracted from any given wave to depend
solely on the characteristics of that wave; it may also depend on the
other waves and on the mean flow.

The following analysis is designed to compute the absorption of energy from linear internal waves by a turbulent boundary layer. The analysis assumes the waves to be large compared to the boundary layer and uses the observed wave motions at a particular frequency to compute the turbulent stresses acting on these motions. No assumption concerning the source of these stresses is made; they may be due to motions at other frequencies.

Below, the relevant internal wave and boundary layer scales will be computed, and the equations of motion simplified for these scales. The resulting equations will be used to interpret the structure shown in figure 11; the first qualitatively, and then quantitatively by computing the energy absorption from the near inertial waves.

Wave scales

The vertical scales of internal waves in the thermocline away from the inertial frequency are well known (Garrett and Munk, 1979). The vertical scales of near inertial waves, particularly in the deep ocean, are less well characterized. Munk and Phillips (1968) suggest that they may be modeled as horizontally propagating internal wave modes which are near their northern turning latitude. In such a model the vertical structure of each mode is independent of latitude, so the near inertial vertical wavenumber spectrum is determined by the high frequency (relative to f) wavenumber spectrum at lower latitudes. Fu (1980), following Munk and Phillips (1968), shows that this approach accurately models the observed near inertial energy spectra in the deep North

Atlantic. One result of his analysis is that the near inertial vertical

wavenumber spectrum should be similar to that at higher frequencies, with,

however, less energy in the low mode waves, as these have a more south-

erly turning latitude. The inverse analysis of the IWEX experiment

(Müller et al., 1978), consistent with this prediction, finds little

energy at the lowest 3 modes for near inertial motions; these modes con-

tain significant energy only at higher frequencies.

The vertical near inertial wave scales will be estimated using

the GM75 (Garrett and Munk, 1975) wavenumber spectrum with the addition

of a low wavenumber cutoff. The wavenumber spectrum is given by

$$A(\lambda) = \frac{1.5}{[1 + (\lambda - d)]^{2 \cdot 5}} \qquad \lambda > d \qquad (1)$$

$$= 0 \qquad \lambda < d$$

where $\lambda = \beta/\beta^*$ for vertical wavenumber β and, $\beta^* = j^*\pi N/bN_o$,

$b = 1.3$ km, $N_o = 3$ cph, $j^* = 6$, and $d = j_p/j^*$. The low mode cutoff

j_p is taken as 3, following Müller et al. (1978). Using a local

Väisälä frequency $N = .45$ cph, the characteristic vertical wavenumber

β^* is found to be 2.2×10^{-3} or $(460 \text{ m})^{-1}$. The smallest energetic

wavenumber is $j_p/j^* \beta^*$ or $(920 \text{ m})^{-1}$. Integrating (1) 45 per cent of

the energy is found at wavenumbers less than β^*, 90 per cent of the

energy is found at wavenumbers less than $4\beta* = (115 \text{ m})^{-1}$. For typical

mixed layer height of $H = 20$ m, $\beta*H$ has a value of .04, with 90 per

cent of the wave energy having $\beta H < .17$. The boundary layer is thin com-

pared to the vertical scale of the energetic waves.

Horizontally, Fu (1980) finds near-inertial wave scales larger than

20 km for the energy containing waves. The interaction of the waves and

boundary layer will also be modulated by the horizontal boundary layer

scales. Armi and D'Asaro (1980) find gross boundary layer characteristics

varying on scales 10 km or larger. Both these scales are much larger than

the boundary layer height.

Equations of motion

The horizontal x momentum equation for an f plane, turbulent,

Boussinesq fluid with no mean velocity can be written

$$\underbrace{\frac{\partial u}{\partial t}}_{\frac{1}{fT}} + \underbrace{\vec{u} \cdot \vec{\nabla} u}_{\frac{u}{fL}} - \underbrace{fv}_{1} = -\frac{\partial P}{\partial x} \quad \frac{u*^2}{fuH}\left[\underbrace{-\frac{\partial}{\partial z}(\overline{u'w'})}_{1} - \underbrace{\frac{\partial}{\partial x}(u'^2)}_{\frac{10H}{L}} - \underbrace{\frac{\partial}{\partial y}(\overline{u'v'})}_{\frac{H}{L}} \right] \quad (2)$$

where turbulent stresses have been scaled by values typical of a two-

dimensional turbulent boundary layer (Townsend, 1976, pg. 290) and the

mean density has been absorbed into P. For near inertial waves inter-

acting with a turbulent boundary layer of typical height (H = 20 m) and

typical wave velocity (u = 1 cm/s), length (L = 20 km), and time

(T = 1/f = 10^4s) scales the following non-dimensional numbers are small: $\frac{u}{fL}$ = .005, 10 H/L = .01. The horizontal momentum equations can now be written:

$$\frac{\partial u}{\partial t} - fv = -\frac{\partial P}{\partial x} - \frac{\partial \overline{u'w'}}{\partial z} \tag{3}$$

$$\frac{\partial v}{\partial t} + fu = -\frac{\partial P}{\partial y} - \frac{\partial \overline{v'w'}}{\partial z} \tag{4}$$

The magnitude of P can be estimated by Fourier transforming (3) and (4) $w = \int \hat{w}\, e^{i(kx + \ell y - \sigma t)}$ and solving for the kinetic energy

$$(\sigma^2 - f^2)^2\,[|\hat{u}|^2 + |\hat{v}|^2] = (\sigma^2 + f^2)(k^2 + \ell^2)\,|\hat{P}|^2 \tag{5}$$

so that

$$P = \frac{uL\,(\sigma^2 - f^2)}{(\sigma^2 + f^2)^{\frac{1}{2}}} \tag{6}$$

Note that the pressure gradients above the boundary layer become very small near the inertial frequency.

Armi and D'Asaro (1980) conclude that on the time scale of several days or shorter the temperature fluctuations observed at a fixed mooring are primarily due to horizontal and vertical advection. Turbulent mass transport becomes important only on a longer time scale. Making this assumption the appropriate mass conservation equation for the super-inertial motion is

57

$$\rho = \bar{\rho}_z \, \xi \tag{7}$$

$$\xi_t = w \tag{8}$$

where ξ is the vertical displacement and $\bar{\rho}$ is the mean density. The non-linear terms have been eliminated as from (2) above.

The vertical momentum equation can be written

$$\frac{\partial P}{\partial z} = - [\xi_{tt} + N^2 \xi] - [\frac{\partial}{\partial z}(\overline{w'^2})] \tag{9}$$

$$N^2 = - g \, \frac{\partial (\ln \bar{\rho})}{\partial z} \tag{10}$$

where N is the Väisälä frequency, (7) has been used, and the non-linear and horizontal stress divergence terms have been eliminated as in (2) above.

In the absence of turbulent stresses, equations (3), (4), (7), (8), and (9) are the equations for inviscid linear internal waves. For a constant N they have solutions of the form $e^{i\beta z}$, where β is the vertical wavenumber. In the presence of stresses the pressure change across the boundary layer is given by the sum of the two terms in (9). The vertical displacement ξ is strongly constrained by the ocean bottom at $z = 0$ and the internal wave displacements above the mixed layer. The fractional pressure change across the boundary layer of thickness

H due to the first term in (9) should thus be similar to that in the
inviscid case, βH, and thus be small. The fractional change in pres-
sure due to the second bracketed term in (9) has a magnitude
$u*^2/(\sigma - f)uL < 10^{-2}$ using (6) to estimate P, and $\sigma > 1.03f$,
$u* < .2$ cm/s. The fractional change in pressure across the boundary
layer is thus small. This results primarily from the large vertical
scale of the near inertial waves, relative to the boundary layer
thickness.

Scaled equations

The scaled equations for motions near the inertial frequency
are

$$-i\sigma \, \hat{u} - f \, \hat{v} = - \frac{\partial \hat{P}}{\partial x} - \frac{\partial \, \widehat{\overline{u'w'}}}{\partial z} \tag{11}$$

$$-i\sigma \, \hat{v} + f \, \hat{u} = - \frac{\partial P}{\partial y} - \frac{\partial \, \widehat{\overline{v'w'}}}{\partial z} \tag{12}$$

$$\frac{\partial P}{\partial z} = 0 \tag{13}$$

$$\frac{\partial \hat{u}}{\partial x} + \frac{\partial \hat{v}}{\partial y} + \frac{\partial \hat{w}}{\partial z} = 0 \tag{14}$$

where the caret denotes a Fourier transform in time only. These
equations are appropriate for a thin domain stretching from the ocean
bottom $z = 0$, tc just above the boundary layer. Note that the stress
terms in (11) and (12) are the components of turbulent stress divergence
with frequency σ, not the total stress divergences.

59

These equations can be used to evaluate the interaction of the boundary layer and the wave motions at frequency σ. Consider a level z_o above the boundary layer chosen so that the stress terms in (11) and (12) are negligible. Since the pressure is constant across the boundary layer, the pressure terms in (11) and (12) can be evaluated from the velocity field at z_o, yielding equations for the boundary layer stresses in terms of the velocity field.

$$- \frac{\partial \overline{\hat{u'w'}}}{\partial z} = -i\sigma(\hat{u} - \hat{u}_o) - f(\hat{v} - \hat{v}_o) \tag{15}$$

$$- \frac{\partial \overline{\hat{v'w'}}}{\partial z} = -i\sigma(\hat{v} - \hat{v}_o) + f(\hat{u} - \hat{u}_o) \tag{16}$$

where $\hat{u}_o$, $\hat{v}_o$ are velocity components measured at z_o.

Equations (15) and (16) state that the presence of boundary layer stresses leads to different velocities within the boundary layer than above it, even though the pressure field is the same. They state that <u>all observed velocity shears within the boundary layer are due to tur-bulent stresses</u>. This is the usual assumption in boundary layer analysis. For low frequency motions, $\sigma \ll f$, (15) and (16) become the steady Ekman layer equations with a three way balance of Coriolis force, $f\hat{u}$; pressure gradient, $f \hat{u}_o$; and turbulent stresses (Priestly, 1959, pg. 34). For internal wave motions, however, $\sigma \gtrsim f$, so the additional terms in (15) and (16) must be included.

60

Energy equation

Equations (15) and (16) allow the turbulent stresses which act upon the motions at frequency σ to be computed from the velocity field. It is precisely these stresses that may absorb energy from the internal wave motions, and thus act to dissipate the waves. Multiplying (11), (12) and the Fourier transform of (9) by $\hat{u}^\dagger$, $\hat{v}^\dagger$ and $\hat{w}^\dagger$ respectively, (the dagger denotes complex conjugation), summing the products, adding the complex conjugate of the sum and using (14), an energy equation is derived:

$$\text{Re } \{\vec{\nabla} \cdot (\vec{u}^\dagger \, \hat{P})\} = -\text{Re } \{\hat{u}^\dagger \frac{\partial}{\partial z} (\widehat{u'w'}) + \hat{v}^\dagger \frac{\partial}{\partial z} (\widehat{v'w'}) + \hat{w}^\dagger \frac{\partial}{\partial z} (\widehat{w'^2})\}. \quad (17)$$

where $\text{Re } \{x\}$ is the real part of x. Equation (17) states that for motions at frequency σ the energy flux divergence is equal to the rate of working by the boundary layer stresses on the velocity field.

In the Appendix the work done by the third term on the RHS of (17) is shown to be small compared to that done by the first two terms. The turbulent stress divergences can be evaluated using (15) and (16) which yields

$$\left\{\begin{array}{l}\text{Work per unit volume}\\[4pt]\text{per unit time done by}\\[4pt]\text{stresses on motions}\\[4pt]\text{at frequency } \sigma\end{array}\right\} \begin{array}{l}= (\sigma - f) \text{ Im } \{\hat{c}(\sigma) \, \hat{c}_o^\dagger(\sigma)\}\\[8pt]\quad - (\sigma + f) \text{ Im } \{\hat{c}(-\sigma) \, \hat{c}_o^\dagger(-\sigma)\}\end{array} \quad (18)$$

$$\hat{c} = (\hat{u} + i\hat{v})/\sqrt{2} \qquad\qquad (19)$$

where $\hat{c}(\sigma)$ is a complex velocity vector, corresponding to clockwise motion for positive σ and anticlockwise motion for negative σ. $\hat{c}_o(\sigma)$ is evaluated at the reference height z_o, above the boundary layer.

Chapter 8. Interpretation of near inertial observations

General features

The observed near inertial structure is shown in figure 11. Near

inertial motions have less energy within the mixed layer than in the

interior. Equations (15) and (16) require that all differences in

velocity be due to turbulent stresses. The observations thus require

turbulent stresses to fill the mixed layer, assuming no turbulent stress-

es in the interior. Note that a random, statistically steady stress

field will have an average inertial component of zero and thus will not

affect the near inertial energy level. At any time such a stress field

is as likely to increase the local near inertial amplitude as decrease it.

Consistently less near inertial energy within the mixed layer indicates

a variation of the boundary layer stresses phase locked with the near

inertial motions, i.e., the boundary layer stresses are modulated by the

near inertial wave motions.

Equation (17) gives the energy absorbed by the boundary layer from

the near inertial motions. Note that the presence of stresses alone

does not lead to energy absorption. For this the stresses must be cor-

related with the motion so that work is done. Equation (18) expresses

this same energy absorption as the sum of terms involving the clockwise

and anticlockwise components of the velocity field at frequency σ.

Each term is proportional to the quadrature spectrum of the motion

within the boundary layer with that at some reference level outside the

boundary layer. The quadrature spectrum can be expressed as

$$\text{Im } \{\hat{c} \; \hat{c}_o^\dagger\} = |c| |c_o| \; \gamma \sin \theta \qquad (20)$$

where γ and θ are the coherence and phase of the boundary layer velocity with respect to the reference velocity. Since $0 < \gamma < 1$ the sign of the energy transfer between the wave velocities and the turbulent stresses is determined by the sign of the phase, as shown in table 2. These results, for the case of energy absorption alone, have been derived by Munk et al. (1970) for a laminar Ekman layer. Their results are here shown to be determined on purely energetic grounds.

The observations in figure 11 show the boundary layer near inertial clockwise velocities leading the interior. By table 2 this implies energy absorption by the boundary layer from internal wave motions with $\sigma > f$, and/or energy flux into motions with $\sigma < f$. Note that although the turbulent stresses fill the mixed layer, they only exchange energy with the waves in the lower part of the mixed layer.

Energy flux calculation

The total work done by the boundary layer stresses on the motions at frequency σ, per unit area per unit time, $\Pi(\sigma)$, is found by integrating (18) across the boundary layer.

$$\Pi(\sigma) = \int_o^{z_o} \text{Im}\{(\sigma - f)\hat{c}(\sigma,z)\hat{c}^\dagger(\sigma,z_o)\}dz - \int_o^{z_o} \text{Im}\{(\sigma + f)\hat{c}(-\sigma,z)\hat{c}^\dagger(-\sigma,z_o)\}dz$$

$$(21)$$

Table 2

Energy flux and boundary layer phase

<u>Clockwise motion</u>

$\sigma > f$ $\sigma < f$

B.L. leads → absorption   B.L. leads → production

B.L. lags → production   B.L. lags → absorption

<u>Anticlockwise motion</u>

<u>all σ</u>

B.L. leads → absorption

B.L. lags → production

Lead and lag are relative to the direction of rotation

65

Equation (21) is used below to compute the flux of near inertial wave energy into the benthic boundary layer.

For near inertial motions the spectral estimates $\hat{C}(\sigma, z)$ in (21) must be evaluated with a high frequency resolution to resolve $\sigma - f$. $\hat{C}(\sigma)$ is therefore computed for each instrument using a 1024 element Fourier transform acting on a single 92 day Hamming windowed piece (Harris, 1978). The raw data is averaged and subsampled over 127.5 minutes before Fourier transforming, resulting in a variance reduction of approximately 5 per cent at .05 cph. This processing yields estimates of $\hat{C}(\sigma)$ with a frequency resolution of approximately .01f. For a given instrument pair $\text{Im}\{(\sigma - f)\hat{C}_1\hat{C}_2^\dagger\}$ is computed for each spectral estimate, these products are then averaged over frequency to increase the statistical reliability of the estimate. This processing yields spectral averages at a fixed height off the bottom and ignores any variations in mixed layer height. For a record of only 92 days length, this is unavoidable. The calculation also ignores any Doppler shifting of the wave frequency by the mean current.

The integrands in equation (21) are functions of both frequency and the pair of instruments used. The frequency dependence will be examined first. In figure 12b the reference level z_o is chosen as 55 m and the energy flux resulting from the clockwise term in (21) is plotted for $z = 15$ m as a function of frequency. The solid line shows the results; the dashed lines give 95% confidence limits computed using the phase confidence limits given by Koopmans (1974, pg. 285). The computed

energy flux is indistinguishable from zero at frequencies above .08 cph. Some energy absorption is indicated at the M_2 tidal frequency. Near the inertial frequency significant energy absorption is indicated for $\sigma > f$; significant production of energy is indicated for $\sigma < f$. Frequencies below .02 cph are not well behaved; the magnitude of the energy transfer varies widely with frequency and details of the calculation procedure. They are not shown in figure 12.

Figure 12a shows the same computation with $z_0 = 65$ m, $z = 55$ m. Both these levels are above the boundary layer and as expected there is no energy absorption indicated. The same calculation for the anticlockwise term in (21) shows a weak pattern of energy absorption within the boundary layer and near the inertial frequency.

The integration required by equation (21) is shown in figure 13 for two near inertial frequency bands. The results are tabulated in table 3. Figure 13a shows the integration of the clockwise term for a band extending from the inertial frequency .04 cph, to .069 cph. Each curve in 13a plots the integrand from (21), i.e., the energy flux per unit volume, as a function of z for a fixed reference height z_0. The area under each curve gives the energy flux per unit area. The solid vertical lines are selected 95 per cent confidence limits. Figure 13a indicates significant energy absorption for $z < 20$ m for all reference levels. The double diagonal line, a rough average over all reference levels, yields an energy absorption rate of .015 ergs/cm^2/s. Notice
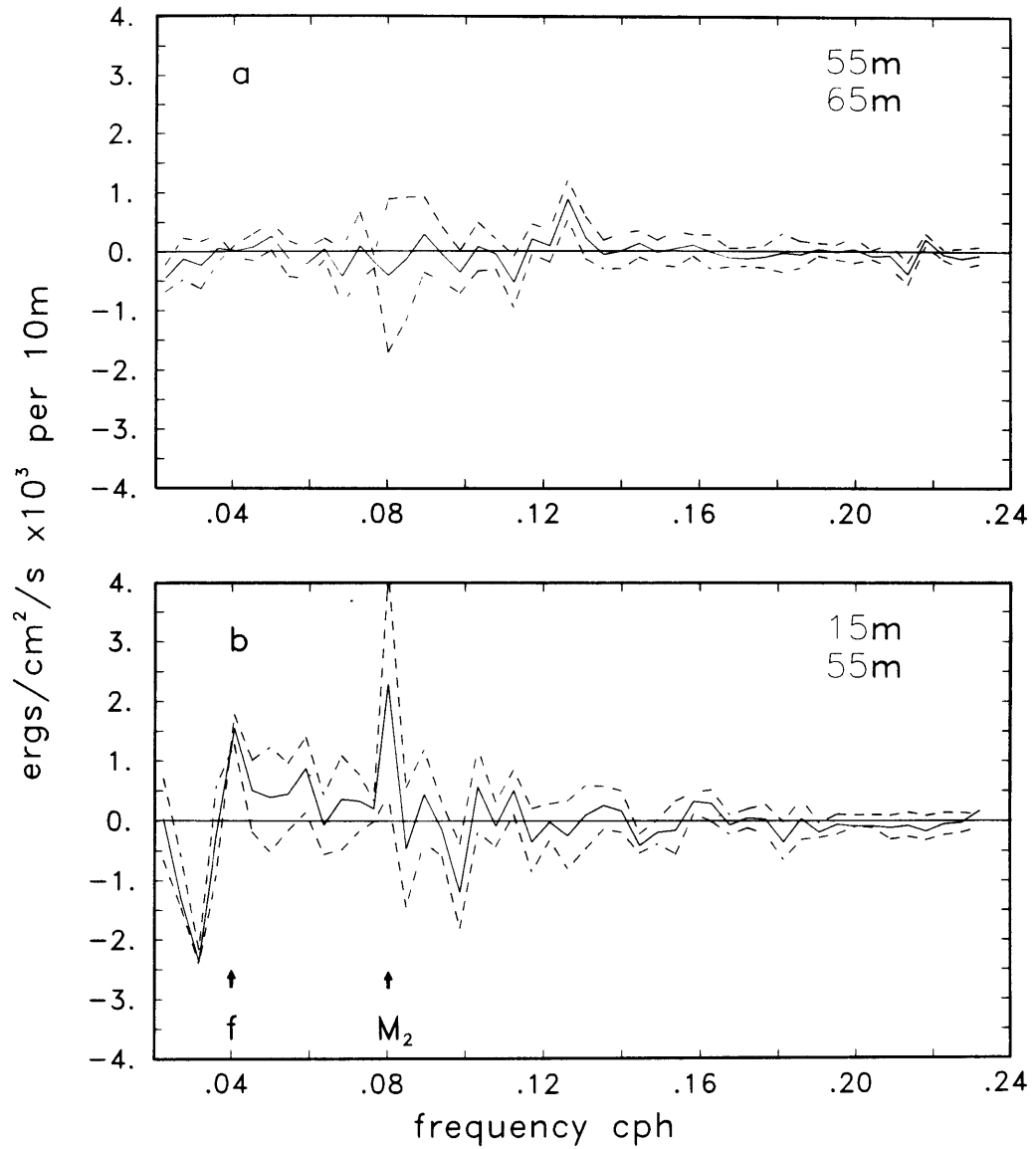
Figure 12

Energy absorption density by turbulent boundary layer as computed from equation (21) for the clockwise velocity component. The 95% confidence limits computed from phase confidence limits are shown as dashed lines.

a) Reference instrument at 65 m, z = 55 m;

b) Reference instrument at 55 m, z = 15 m.

Figure 13

Computation of near inertial energy absorption rate per unit area by
boundary layer using equation (21). Each figure plots an integrand of
(21) versus height for 5 different reference levels, 35 m to 85 m. The
area under each curve gives the estimated energy absorption. The clock-
wise (figures a, c) and anticlockwise (figures b, d) contributions are
shown for two near inertial frequency bands.

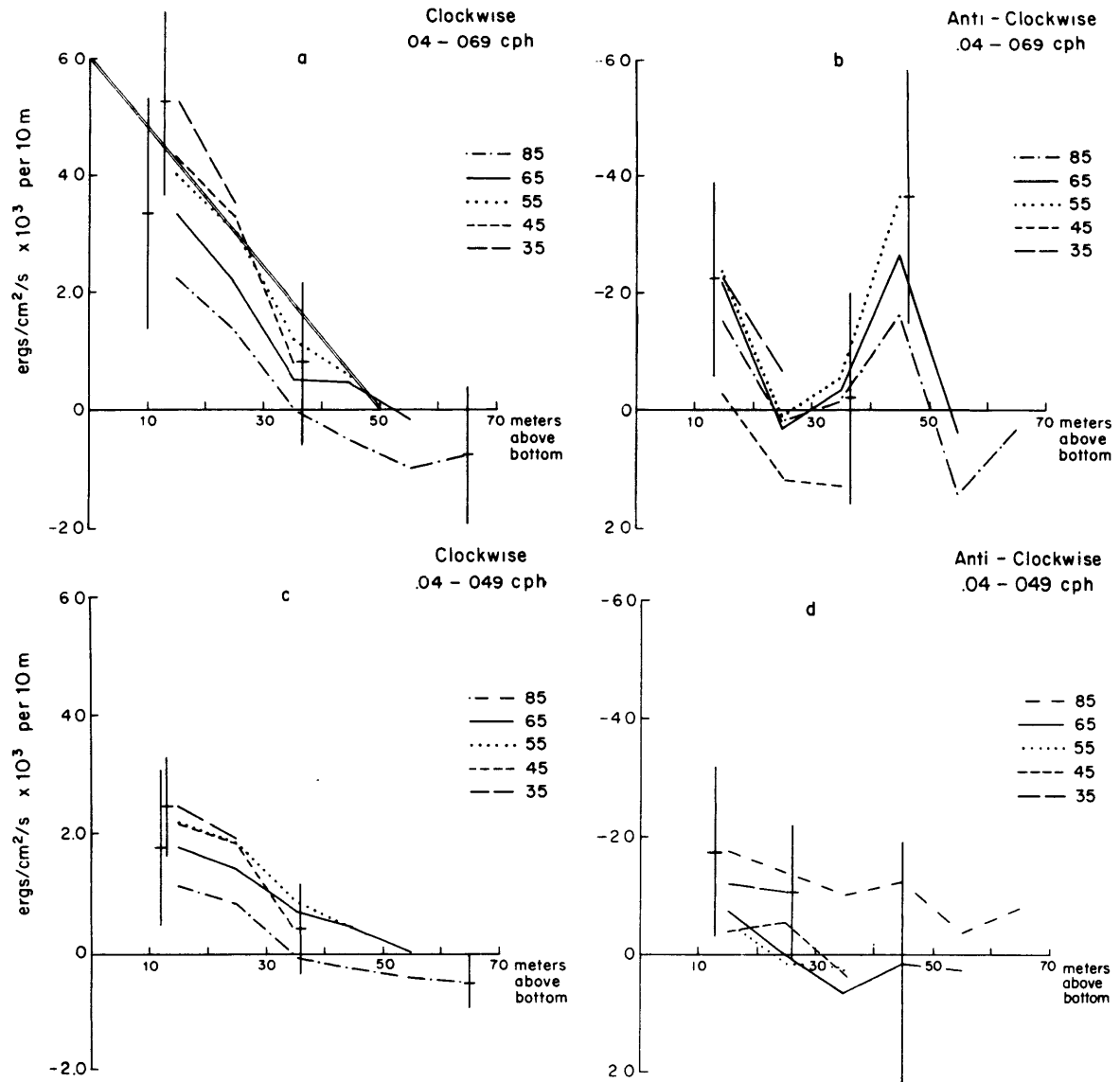however, that a large contribution to this integral occurs for

$z < 15$ m, where there is no data. Fortunately, the contribution from

this region can be bounded by noting that the vertical coordinate in

figure 13a is a quadrature spectrum and by equation (20) is bounded above

by $\left| (\sigma - f) \hat{C}(\sigma,z) C^{\dagger}(\sigma,z_o) \right|$. Estimating this by $(\sigma - f) \left| C(\sigma,z_1) \right|^2$,

$z_1 = 15$ m, yields a maximum value of the vertical coordinate of

$.018$ ergs/cm^2/s per 10 m. If the diagonal line in 13a is bent at

$z_1 = 15$ so that it intersects 18 at $z = 0$ an estimate of

$.024$ ergs/cm^2/s for the energy absorption is found. This value is

probably an overestimate. A lower bound can be estimated from the area

under a diagonal line from 30 m on the horizontal axis to

$.003$ ergs/cm^2/s per 10 m on the vertical axis. This yields

$.004$ ergs/cm^2/s.

Figure 13b shows the same calculation for the anticlockwise term

in (21). The individual curves show a strong peak at 45 m. As dis-

cussed above the instrument at 45 m is believed to exhibit a directional

bias of up to 10° relative to the instruments at 55 m and 65 m for un-

known reasons. The peak at 45 m is likely due to instrumental effects,

and is not included in the integration. This effect is more pronounced

for the anticlockwise motions than for the clockwise motions, due to

the smaller anticlockwise phases.

Figures 13c, d show the same calculation for a narrower frequency band, .04-.049 cph. The clockwise terms, figure 13c, have less error and larger coherences and phases than for the wider band, figure 13a. The anticlockwise terms, figure 13d, however, are barely distinguishable from zero and show much less order than in figure 13b.

Internal wave energy absorption

The calculation outlined above yields the energy absorption rates shown in table 3. The results are shown for two near inertial frequency bands, along with estimated errors. These errors are dominated by the lack of measurements below 15 m, although the finite record length also makes a contribution.

The array used in this experiment is short compared to typical vertical internal wave scales. Given the instrumental errors and the significant phase differences attributed to turbulent stresses, the array yields no information on the vertical structure of the deep ocean internal wave field. The spectral shape and energy level of the observed superinertial fluctuations are similar to the universal internal wave forms. This alone suggests that these fluctuations should be attributed to internal waves, and the calculated energy flux be included in the internal wave field energy budget.

The above calculation yields energy fluxes between the boundary layer and superinertial and subinertial, clockwise and anticlockwise motions. Which of these fluxes should be included in the energy budget for internal waves? The superinertial clockwise motions are most

71

likely due to internal waves and the flux of energy associated with them
will be included in the internal wave energy budget. As noted in
chapter 5, the near inertial anticlockwise motions show far more energy
than would be predicted by internal wave theory. This suggests that
these motions are not due to internal waves. The associated energy flux
will not be included in the internal wave energy budget.

The above calculation suggests an energy flux into the subinertial
motions, as shown in figure 12b. The change in the sign of the computed
energy flux at the inertial frequency is due to the change in sign of
$(\sigma - f)$ in equation (21); the sign of the relative phase of the boundary
layer and interior motions remains unchanged. Motions with $\sigma \ll f$ are
believed to be highly nonlinear and quasigeostrophic (Rhines, 1979);
motions with $\sigma > f$ are believed to be linear internal waves. The
dynamics of slightly subinertial motions is unclear. Since the calcu-
lation used above assumes a linear momentum equation, it may not cor-
rectly estimate the energy flux for $\sigma < f$.

The above calculation also assumes no mean velocity. Doppler shif-
ting of the wave frequency by the mean velocity will result in some
superinertial wave energy at subinertial frequencies. The calculation
will compute the wrong energy flux for these waves. The computed energy
flux at slightly subinertial frequencies will not be included in the
internal wave energy budget.

Only the calculated energy flux from near inertial clockwise
motions will be used in the following calculations. This should yield
the best estimate of the effect of the benthic boundary layer on the
internal wave field. Including the anticlockwise or subinertial energy
absorption in the internal wave energy budget could have a significant

72

effect on the estimated energy fluxes (c.f. table 3, figure 12). The

anticlockwise motions would increase the total wave energy absorption;

the subinertial motions would decrease it.

Results of calculations

The calculated energy fluxes are shown in table 3. Over the

period of this experiment the boundary layer absorbs roughly $\Pi =$

$.015$ ergs/cm^2/s from the near inertial internal wave field. This is a

net flux. Although generation of internal waves by the boundary layer

may be occurring (Townsend, 1965), absorption of near inertial waves

generated elsewhere dominates, resulting in a net absorption of near

inertial energy.

The calculated clockwise energy absorption rate has been used to

compute a wave reflection coefficient

$$|R(\sigma)|^2 = \frac{F_+(\sigma)}{F_-(\sigma)} = 1 - \frac{\Pi(\sigma)}{F_-(\sigma)} \tag{22}$$

where F_+, F_- are the upward and downward internal wave energy fluxes

respectively. The downward energy flux F_- can be estimated from

$$F_- = C_g \frac{E(\sigma)}{2}$$

$$= \frac{\sigma^2 - f^2}{\sigma\beta} \frac{E(\sigma)}{2} \tag{23}$$

73

Table 3

	.04 - .069 cph	.04 - .049 cph
Absorption of Energy (ergs/cm^2/s)		
Clockwise	.015	.007
	.004 - .025	.003 - .012
Anticlockwise	.007	.005
	.004 - .017	0 - .008
Downward Energy Flux (ergs/cm^2/s)	.35	.12
Reflection Coefficient	.96	.94
	.99 - .93	.975 - .9
Clockwise Relaxation Time (days)	1.4	2.4
	4.6 - .84	5.5 - 1.3

where C_g is the vertical component of internal wave group velocity (Lighthill, 1978, chapter 4). $|R|^2$ is assumed to be close to 1 so that roughly half of the internal wave energy $E(\sigma)$ is propagating downward. Equation (23) is evaluated using the same technique used to evaluate the integrands of (21). A value of $\beta = \beta* = (460 \text{ m})^{-1}$, roughly the value of β^{-1} weighted by the spectrum (1), is used. The resulting values of F_- and $|R|^2$ are shown in table 3. The reflection coefficient is roughly .95 so that 5 per cent of the wave energy is absorbed in each reflection.

Another useful measure of the energy absorption rate is the boundary layer relaxation time

$$\tau_R = \frac{E(\sigma) \ H}{\Pi(\sigma)} \tag{24}$$

which gives the time required for the observed energy absorption rate to reduce the observed kinetic energy within the boundary layer of height H to zero, if there were no energy input. Unlike the reflection co-efficient, τ_R depends only on boundary layer properties and does not require any knowledge of the wave properties. Evaluating (24) yields relaxation times of several days.

Chapter 9. Slab model of the boundary layer

In the previous section the absorption of internal wave energy by the benthic boundary layer was computed. Below the physics responsible for this absorption is examined. A simple slab model with a linearized quadratic drag law will be shown to account for most of the observed internal wave/boundary layer interactions.

Equations

Consider a mixed layer of height H, uniform in velocity and density above a flat bottom, and underlying a region with constant Väisälä frequency N (Figure 14). A constant velocity U is imposed in the +x direction. Above the mixed layer the fluid is inviscid. The observed mixed layers are generally capped by a density change of order $\dfrac{\Delta\rho}{\rho} \sim N^2 H$. Since $\beta H \ll 1$ for vertical wavenumbers, β, typical of the deep ocean, this density step is dynamically insignificant (D'Asaro, 1978), and not included in the model.

The observations presented here clearly indicate the presence of turbulent stresses throughout the mixed layer. Their structure within the mixed layer is less clear, particularly as no measurements were taken within 15 m of the bottom. An integral model of the boundary layer will thus be used. Within the mixed layer the turbulent stresses, $\vec{\tau}$, are assumed to decay linearly from their bottom value $\vec{\tau}_o$ to zero at z = H. $\vec{\tau}_o$ acts to oppose the instantaneous mixed layer velocity and has magnitude $|\tau_o| = u*^2 = C_D S^2$, where S is the instantaneous mixed layer speed. The linearized Boussinesq equations for the perturbation quantities in the mixed layer are:
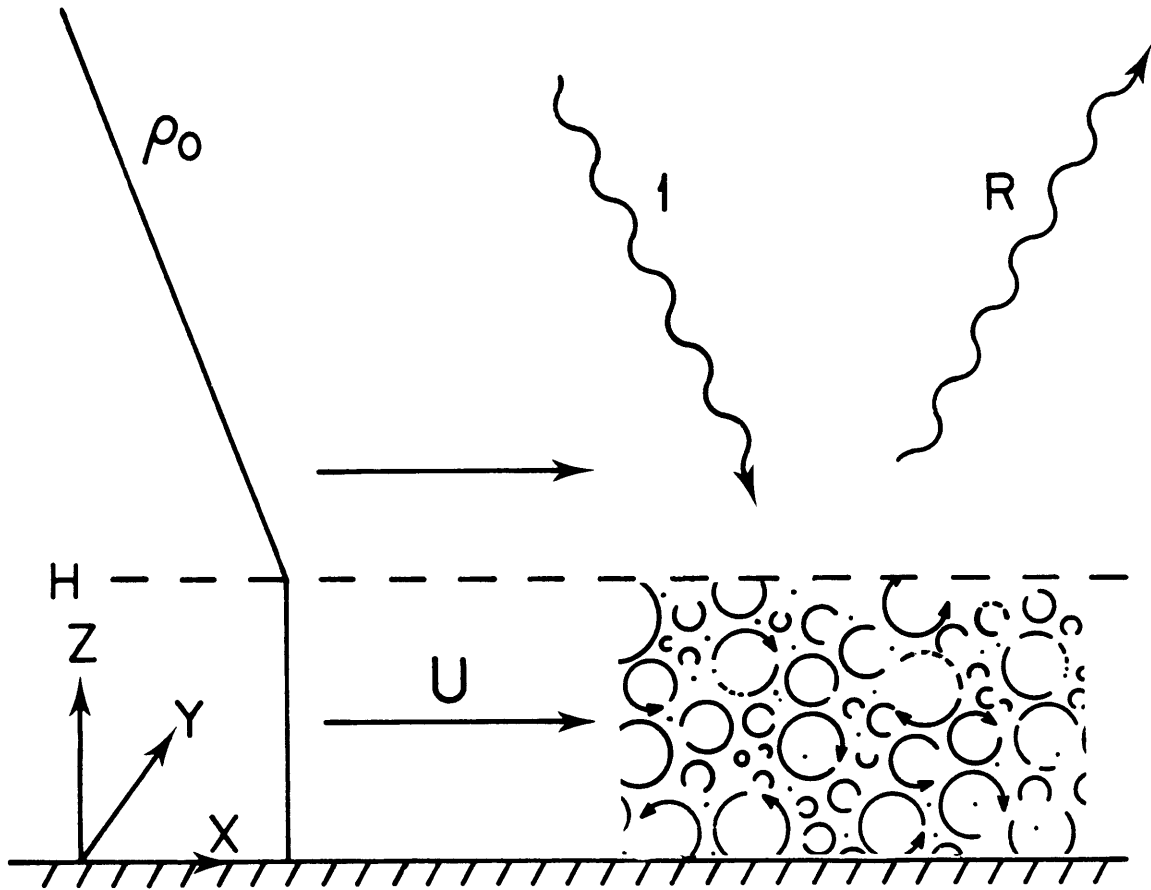
Figure 14

Slab model of internal wave interaction with boundary layer. The mixed
layer is uniform in density and velocity with a drag applied to it at
the ocean bottom. The interior is inviscid, with constant N, and a
downward propagating wave reflecting from the mixed layer.

$$\frac{\partial u}{\partial t} - fv = -\frac{\partial P}{\partial x} - 2ru \qquad (25)$$

$$\frac{\partial v}{\partial t} + fu = -\frac{\partial P}{\partial x} - rv \qquad (26)$$

$$\frac{\partial u}{\partial x} + \frac{\partial v}{\partial y} + \frac{\partial w}{\partial z} = 0 \qquad (27)$$

where $r = \dfrac{C_D U}{H}$ results from linearizing the drag law, and P denotes the pressure divided by density. Within the mixed layer u, v, P and $\frac{\partial w}{\partial z}$ are constant and since $w(0) = 0$, $\frac{\partial w}{\partial z} = \frac{w(H)}{H}$. The mixed layer velocities are completely determined by the value of P at $z = H$. This model is similar to that of Fu (1980), although he does not include a mean current.

In the interior equations (25) - (27) apply with $r = 0$ and

$$\frac{\partial w}{\partial t} + N^2 \xi = -\frac{\partial P}{\partial z} \qquad (28)$$

$$\frac{\partial \xi}{\partial t} = w. \qquad (29)$$

These are the well known internal wave equations (Garrett and Munk, 1979). Assuming that all quantities vary as $e^{i(kx + \ell y - \sigma t)}$ interior equations have a solution of the form

$$P = e^{i\beta z} + Re^{-i\beta z} \qquad (30)$$

78

$$\beta^2 = (k^2 + \ell^2)(N^2 - \sigma^2)/(\sigma^2 - f^2) \tag{31}$$

This corresponds for $\beta > 0$ to a downward propagating internal wave of unit amplitude and an upward propagating wave of amplitude R. The equations can be solved by requiring P and w to be continuous at z = H.

Solving the mixed layer and interior equations separately for w(H) in terms of P yields:

$$\frac{1 - R}{1 + R} = - \frac{\sigma}{\beta\ H(\sigma^2 - f^2)} \frac{\sigma^2 - f^2 - 2r^2 + 3\ ir\sigma}{r(1 + \sin^2 \theta) - i\sigma} \tag{32}$$

where $\sin \theta = \ell/(k^2 + \ell^2)^{\frac{1}{2}}$.

Solving (25) and (26) for $|u|^2 + |v|^2$ in terms of P with and without r, yields the ratio of kinetic energy within the mixed layer to that immediately above it.

$$\frac{(|u|^2 + |v|^2)_{ML}}{(|u|^2 + |v|^2)_{INT}} = \qquad \cdot$$

$$\frac{(\sigma^2 - f^2)^2}{(\sigma^2 + f^2)} \frac{\sigma^2 + f^2 + r^2(1 + 3 \sin^2 \theta) - 2rf \sin \theta \cos \theta}{(\sigma^2 - f^2 - 2r^2)^2 + 9r^2 \sigma^2} \tag{33}$$

A similar calculation yields the cross spectra for the clockwise component of motion

$$C_{ML}(\sigma)\; C_{INT}^{\dagger}(\sigma) =$$

$$\frac{\sigma + f - r\sin\theta\cos\theta + ir(1 + \sin^2\theta)}{(\sigma - f)[\sigma^2 - f^2 - 2r^2 + 3ir\sigma]} \frac{(k^2 + \ell^2)}{2} |P|^2 \qquad (34)$$

The relaxation time τ_R defined by (24) can be computed by forming an energy equation yielding

$$\tau_R = \frac{1}{2r} \frac{\sigma^2 + f^2 - 2rf\sin\theta\cos\theta + r^2(1 + 3\sin^2\theta)}{\sigma^2 + f^2 + \sigma^2\cos^2\theta + f^2\sin^2\theta + 2r^2(1 + \sin^2\theta)} \qquad (35)$$

Results

The slab model has one parameter, $r = C_D U/H$. Using $U/u^* = 32$, $H = 20$ m, $U = 7$ cm/s yields $r = 3.4 \times 10^{-6}$ sec^{-1}. Note that $r \ll f$. For a given incident internal wave specified by a frequency σ, a vertical wavenumber β, and a propagation direction θ, the model predicts the boundary layer velocity field, and a wave reflection coefficient R. Since both the interior velocity field at $z = H$, and the boundary layer velocity field are determined by the pressure at $z = H$, all quantities involving just these velocities are independent of the vertical wavenumber of the wave.

Figure 15a plots the relaxation time $\tau_R(\sigma)$ from equation (35). It is somewhat larger than 1 day, and roughly independent of frequency and wave direction. This value is somewhat smaller, but certainly within the range of values calculated from the current meter data (Table 3).

Figure 15

Slab model results plotted versus frequency, for wave orientation $\theta = -90°$, $-45°$, $0°$, $45°$, $90°$ and $r = 3 \times 10^{-6}$.

a) Relaxation time (equation 35).

b) Ratio of horizontal kinetic energy density within mixed layer to energy above mixed layer (equation 33).

c) Phase of clockwise velocity within mixed layer relative to interior (equation 34).

d) Same for anticlockwise velocity.

e) Reflection coefficient for wave energy assuming $\beta = (460 \text{ m})^{-1}$ (equation 32).

Wave Reflection Model   R=3.00E-06
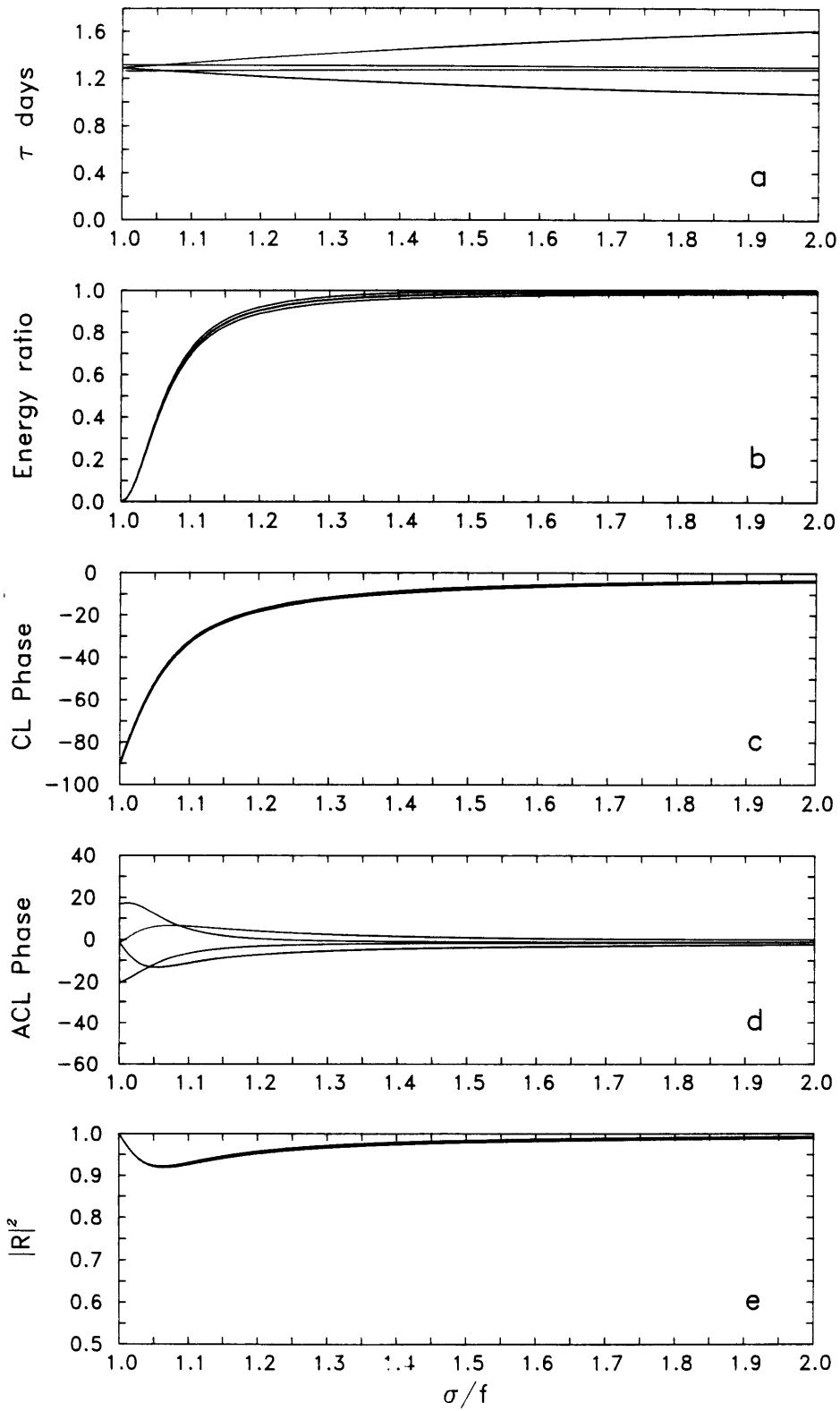
From equation (35) τ_R is seen to be roughly $\frac{1}{3r}$ for $\sigma \sim f$ and

$r/f \ll 1$. This result can be simply derived by forming an energy

equation from equations (25) - (29); the energy absorption rate is seen

to be $r [2|u|^2 + |v|^2]$. If $|u|^2 \simeq |v|^2$ the energy absorption rate is

$3r \dfrac{(|u|^2 + |v|^2)}{2}$, the energy density is $\dfrac{(|u|^2 + |v|^2)}{2}$ so $\tau_R = 1/3r$.

Figure 15b plots the ratio of horizontal kinetic energy in the

mixed layer with that in the interior at $z = H$ (equation (33)). The

results are independent of direction, but strongly frequency dependent.

For $\sigma > 1.3f$ these energies are nearly the same; for $\sigma < 1.3f$, the

boundary layer energy decreases, reaching zero at $\sigma = f$. This behavior

is consistent with the observations which show significantly less iner-

tial energy in the bottommost instruments only for σ near f.

A scale analysis of the momentum equations (25) and (26) explains

the special significance of the inertial frequency. Within the boundary

layer a balance of inertial, frictional and pressure forces exists. The

magnitude of the pressure forces is $u_o(\sigma - f)$ by (6), where u_o is the

typical velocity above the boundary layer. For $\sigma - f \gg r$ the inertial

forces have magnitude σu. The frictional forces, of magnitude ru,

are much smaller since $r \ll f$. The inertial and pressure forces balance,

just as in the interior, and the velocities inside the boundary layer are

the same as above it. The relative magnitudes of the terms in (25) for

$\sigma - f \gg r$ are

$$-i\sigma u - fv = -ikP \qquad -2ru \qquad (36)$$

$$\underbrace{\qquad} \qquad \underbrace{\qquad} \qquad \underbrace{\quad}$$

$$(\sigma - f)u \qquad (\sigma - f)u_o \qquad ru$$

For $\sigma - f \sim r$ this balance can no longer hold and the frictional terms become important. For $\sigma - f \ll r$ they become dominant and a new balance exists

$$\underbrace{\qquad} \qquad \underbrace{\qquad} \qquad \underbrace{\quad}$$

$$ru \qquad (\sigma - f)u_o \qquad ru \qquad (37)$$

The boundary layer velocity u, is much smaller than the interior velocity u_o, their ratio being roughly $(\sigma - f)/r$, as in (33). Physically, the drag forces are small and only become important near the inertial frequency where the inertial forces and pressure gradients in the waves become small.

Figures 15c, d show the relative phase of the boundary layer and interior velocities for clockwise and anticlockwise components respectively. These phases are small except near the inertial frequency, for the reasons discussed above. Near the inertial frequency the boundary layer leads in the clockwise component consistent with energy absorption; the anticlockwise phase is strongly dependent on θ. The predicted clockwise phase is roughly consistent with the observations; figure 3, for example, shows the clockwise phase leading for $\sigma < 1.4f$.

84

The near inertial band anistropy seen in the data can be interpreted as internal wave propagation parallel to the mean flow, i.e., $\theta = 0$. In this case the slab model predicts a leading anticlockwise velocity component in the boundary layer, as observed. If, as seems likely, the anticlockwise velocities are not due primarily to internal wave motions, these model predictions cannot be compared with the observations.

Figure 15e plots the model reflection coefficient, $|R|^2$, as a function of frequency. Unlike the quantities shown in 15a - d, $|R|^2$, depends on the vertical wavenumber of the incoming wave. A value of $\beta = (460 \text{ m})^{-1}$ is used, the same value used in Table 3. The predicted reflection coefficient is significantly less than 1 only near the inertial frequency. It achieves a minimum value of approximately .9, at $\sigma \sim 1.1f$, before rising to 1 at $\sigma = f$. The value of $|R|^2$ computed from the data is consistent with this behavior, showing a significant absorption only near the inertial frequency, with a value of $|R|^2 \sim .95$ (Table 2, figure 3). The predicted behavior of $|R|^2$ can be explained by noting that

$$|R|^2 = 1 - \frac{H}{\tau_R} \frac{E_{ML}}{E_{INT}} \frac{2}{C_g} \tag{39}$$

using (22) - (24). From figure 15a τ_R can be considered constant; E_{ML}/E_{INT} is shown in figure 15b. For $\sigma \gg f$ $E_{ML}/E_{INT} \simeq 1$. C_g, however, varies as $\sigma^2 - f^2$ so that $1 - |R|^2 \sim 1/(\sigma^2 - f^2)$. For $\sigma - f \ll r$, E_{ML}/E_{INT} decreases as $(\sigma^2 - f^2)^2$ (equation (33)) so

$1 - |R|^2 \sim (\sigma^2 - f^2)$. A minimum value of $|R|^2$ therefore occurs for $\sigma \sim f + r$. Physically $|R|^2$ is near 1 for $\sigma \gg f$ because the frictional terms are small. $|R|^2$ decreases as σ approaches f because the group velocity decreases and the small frictional forces have more time to act on the wave. Very near f, the frictional forces decrease the boundary layer velocities and $|R|^2$ increases toward 1.

The least known parameter in the above model is β, the vertical wavenumber. Noting that the group velocity is proportional to β^{-1}, $|R|^2$ is seen to be highly dependent on β (equation 39). Longer waves have a faster group velocity and are absorbed less, while short waves, conversely, are absorbed more strongly. Thus, although the boundary layer may not strongly absorb the internal wave field as a whole, its effect may be much stronger on the shorter, slower internal waves.

Chapter 10. Discussion

The above calculation of near inertial energy flux into the boundary layer is subject to several uncertainties not included in the error bounds. The array used in this experiment is, as mentioned above, too short to provide any vertical wavenumber estimates for the internal wave field. The calculation provides an estimate of energy flux from the near inertial motions into the boundary layer, but does not require the near inertial motions to be related to the internal wave field in midwater. Leaman (1976) finds a near bottom peak in internal wave energy within a few hundred meters of the bottom in this area. This suggests that the dynamics of the near bottom internal wave field may be different from that in midwater, so that the flux measured here cannot necessarily be used in the energy budget of the midwater internal wave field. A related source of uncertainty results from the division of the energy flux into clockwise and anticlockwise sources. As discussed above only the flux resulting from the clockwise near inertial motions is used in the calculations. Similarly, the calculation indicates a significant energy flux out of the boundary layer at slightly subinertial frequencies. This flux has, perhaps incorrectly, not been included in the estimated near inertial wave energy flux. Statistical estimates of these uncertainties are difficult to form, but they probably will not change the sign or general magnitude of the computed flux.

The estimated flux of energy from the internal wave field given above includes only contributions from the near inertial motions. Energy absorption from frequencies above .07 cph has not been included, as the calculated absorption is below the statistical noise. The model presented in chapter 9 suggests that for $\sigma \gg f$ the absorption of internal waves by the boundary layer can be modeled using a constant relaxation time τ_R acting on the wave kinetic energy. Using $\tau_R =$ 2 days, a boundary layer height $H = 20$ m, and an energy of .7 cm^2/s^2 for the band .07 - .45 cph, an energy flux of .008 $ergs/cm^2/s$ is obtained, which adds significantly to the total absorption of internal wave energy.

The relative importance of the near inertial and low frequency motions in the boundary layer energetics can be estimated by comparing the energy fluxes from these two sources. The low frequency turbulent kinetic energy production in the boundary layer is roughly given by integrating $\overline{u'w'}\frac{\partial U}{\partial z}$ across the boundary layer with $\overline{u'w'} = u*^2$ and $\frac{\partial U}{\partial z} = \frac{u*}{kz}$, as appropriate for a logarithmic boundary layer; $k \sim .4$ is von Karman's constant (Hinze, 1959). Integrating from $z = 4\nu/u*$ to a height of 20 m yields a total production of .24 $ergs/cm^2/s$ for $U = 7$ cm/s. This is much more than the energy absorbed from the internal waves. The boundary layer is thus driven primarily by the low frequency geostrophic velocities; the internal waves only modulate it.

The flux of internal wave energy into the boundary layer calculated

here is for one location averaged over 3 months. The model presented in

chapter 9 suggests that this flux should be proportional to the near

bottom current speed. This predicts considerably larger absorption of

the wave energy to the north of this site where the currents are larger

(Schmitz, 1976) and considerably less absorption for regions of low

near bottom speeds. The calculation is probably not relevant to regions

of significant bottom slope or rough topography where the kinematics of

the internal wave field is more complex (Phillips, 1977, chapter 5).

Thus this calculation cannot be used to estimate fluxes in or out of

the internal wave field over rough topography.

Previous observations of near inertial waves have shown a net

downward energy flux (Müller et al., 1978; Leaman, 1976). if the dif-

ference between downward and upward going energy is attributed to absorp-

tion in the boundary layer a reflection coefficient $|R|^2 \sim .5$ is

predicted (Leaman, 1976). The analysis presented here is not consistent

with such a small value of $|R|^2$ and suggests that an alternate

explanation, such as that advanced by Fu (1980) is more correct.

The absorption of internal wave energy by the boundary layer will

act as a net sink of energy for the internal wave field. Assuming an

internal wave energy of 4×10^6 ergs/cm^2 (Garrett and Munk, 1979) a

flux of energy to the boundary layer of .02 ergs cm^2/s will absorb all

the energy in the internal wave field in roughly 6 years. For comparison

an internal wave driven vertical eddy diffusivity of 3×10^{-3} cm^2/s

89

would yield roughly the same wave energy absorption rate (Garrett and Munk, 1979). Estimates of energy input to the internal wave field are generally an order of magnitude larger than the energy absorption rate calculated here (Käse, 1979; Fu, 1980; Bell, 1975). Unless internal wave field relaxation time is much longer than indicated by these estimates, the benthic boundary layer over a flat bottom plays a minor role in dissipating internal wave energy.

Appendix

The third term in (17) $\mathrm{Re}\,\{\hat{w}^\dagger \frac{\partial}{\partial z}(\overline{\hat{w'^2}})\}$ cannot be evaluated from the current meter data, so its magnitude is here estimated and shown to be small. The total energy flux per unit area due to this term is

$$D = \int_0^{z_0} \hat{w}^\dagger(z)\; \frac{\partial\,\overline{\hat{w'^2}}}{\partial z}\; dz \tag{1A}$$

$\hat{w}(z)$ is strongly constrained by $\hat{w}(0) = 0$, and $\hat{w}(z_0)$, the latter being due solely to internal waves. $\overline{\hat{w'^2}}$ will not be larger than $u^{*2} \sim (U/30)^2$. Thus an upper bound for (1A) is

$$D < \left|\hat{w}(z_0)\right|\; u^{*2} \tag{2A}$$

For internal waves (Fofonoff, 1969)

$$\frac{|w|^2}{|u|^2 + |\hat{v}|^2} = \frac{\sigma^2}{N^2}\frac{\sigma^2 - f^2}{\sigma^2 + f^2} \tag{3A}$$

Fu (1980) shows that due to turning point effects, this expression is only valid for $\sigma > 1.02f$; for smaller $\sigma - f$, $|\hat{w}|^2$ is bounded above by (3A) with $\sigma = 1.3f$. Using $\sigma = 1.3f$, $\sigma = .1\,N$, $|u|^2 + |\hat{v}|^2 = 1\ cm^2/s^2$, $U = 7\ cm/s$ yields

$$D < .0027 \quad ergs/cm^2/s \tag{4A}$$

which is less than 20% of total calculated energy absorption from the clockwise term in (18).

91

References

Armi, L., and R. C. Millard, 1976
    The bottom boundary layer of the deep ocean. Journal of Geo-
    physical Research, 81, 27, 4983-4990.

Armi, L., 1977
    The dynamics of the bottom boundary layer of the deep ocean. In:
    Bottom Turbulence, Proceedings of the 8th International Liège
    Colloquium on Ocean Hydrodynamics, edited by J.C.J. Nihoul,
    Elsevier, New York.

Armi, L., and E. D'Asaro, 1980
    Flow structures of the Benthic Ocean. Journal of Geophysical
    Research, 85, Cl, 469-483.

Arya, S. P. S., 1972
    The critical condition for the maintenance of turbulence in stra-
    tified flows. Quarterly Journal of the Royal Meteorological
    Society, 98, 264-273.

Bell, T. H., Jr., 1975
    Topographically generated internal waves in the ocean. Journal of
    Geophysical Research, 80, 320-327.

Biscaye, P. E., and S. L. Eittreim, 1977
    Suspended particulate loads and transports in the nepheloid layer
    of the abyssal Atlantic Ocean. Marine Geology, 23, 155-172.

Blackadar, A. K., and H. Tennekes, 1968
    Asymptotic similarity in neutral barotropic planetary boundary
    layers. Journal of Atmospheric Science, 25, 1015-1020.

Bowden, K. F., 1978
    Physical problems of the benthic boundary layer. Geophysical
    Surveys, 3, 255-296.

Bradshaw, P., 1966
    The turbulence structure of equilibrium boundary layers. NPL
    Aeronautical Report, 1184, Great Britain.

Briscoe, M. G., 1975
    Preliminary results from the Trimoored Internal Wave Experiment
    (IWEX). Journal of Geophysical Research, 80, 27, 3872-3884.

Brown, R. A., 1970
    A secondary flow model for the planetary boundary layer. Journal
    of Atmospheric Sciences, 27 (5), 742-757.

Bryden, H. L., 1976
    Horizontal advection of temperature for low frequency motions.
    Deep-Sea Research, 23 (12), 1165-1174.

Bush, P. A., 1976
    Bathymetry of the MODE-1 region. Deep-Sea Research, 23 (12),
    1105-1113.

Businger, J. A., and S. P. S. Arya, 1974
    The height of the mixed layer in the stably stratified planetary
    boundary layer. Advances in Geophysics, 18A, 73-92.

Caldwell, D. R., and C. W. van Atta, 1970
    Characteristics of Ekman boundary layer instabilities. Journal of
    Fluid Mechanics, 44, 1, 79-95.

Caldwell, D. R., C. W. van Atta, and K. N. Helland, 1972
    A laboratory study of the turbulent Ekman layer. Geophysical
    Fluid Dynamics, 3, 125-160.

Caldwell, D. R., 1976
    Fine-scale temperature structure in the bottom mixed layer on the
    Oregon shelf. Deep-Sea Research, 23, 1025-1035.

Caldwell, D. R., and T. M. Chriss, 1979
    The viscous sublayer of the sea floor. Science, 205 (4411):
    1131-1132.

Calman, J., 1978
    On the interpretation of ocean current spectra: Part I, The
    kinematics of three dimensional vector time series. Journal of
    Physical Oceanography, 8, 4, 627-643.

Csanady, G. T., 1967
    On the "Resistance Law" of a turbulent Ekman layer. Journal of
    Atmospheric Sciences, 24, 5, 467-471.

Csanady, G. T., 1974
    Equilibrium theory of the planetary boundary layer with an
    inversion lid. Boundary Layer Meteorology, 6, 63-79.

Csanady, G. T., 1978
    Turbulent interface layers. Journal of Geophysical Research, 83,
    C5, 2329-2342.

D'Asaro, E., 1978
    Mixed layer velocities induced by internal waves. Journal of
    Geophysical Research, 83, C5, 2437-2438.

93

D'Asaro, E., 1980
Equilibrium scaling of turbulent boundary layers in a pressure gradient. Physics of Fluids, submitted.

Deardorff, J. W., 1970
A three-dimensional numerical investigation of the idealized planetary boundary layer. Geophysical Fluid Dynamics, 1, 377-410.

Falco, R. E., 1977
Coherent motions in the outer region of turbulent boundary layers. The Physics of Fluids, 20, 10, 5124-5132.

Faller, A. J., and R. E. Kaylor, 1966
A numerical study of the instability of the laminar Ekman boundary layer. Journal of Atmospheric Research, 23, 466-480.

Fofonoff, N. P., 1969
Spectral characteristics of internal waves in the ocean. Deep-Sea Research, 16 Supplement, 59-71.

Fu, L. L., 1980
Observations and models of inertial waves in the deep ocean. Ph.D. Thesis, Massachusetts Institute of Technology-Woods Hole Oceanographic Institution Joint Program.

Garrett, C. J. R., and W. Munk, 1975
Space-time scales of internal waves: a progress report. Journal of Geophysical Research, 80, 291-297.

Garrett, C. J. R., and W. Munk, 1979
Internal waves in the ocean. Annual Reviews of Fluid Mechanics, 11, 339-369.

Garwood, R. W., Jr., 1979
Air-sea interaction and the dynamics of the surface mixed layer. Reviews of Geophysics and Space Physics, 17, 7, 1507-1523.

Goldstein, S., 1965
Modern developments in fluid dynamics, Volume 1. Dover Publications, Inc., New York.

Gonella, J., 1972
A rotary-component method for analysing meteorological and oceanographic time series. Deep-Sea Research, 19, 833-846.

Greenspan, H. P., 1968
The Theory of Rotating Fluids, Cambridge University Press.

Gregg, M. C., and M. G. Briscoe, 1979
    Internal waves, finestructure, microstructure and mixing in the
    ocean. Reviews of Geophysics and Space Physics, 17, 7, 1524-1548.

Hamming, R. W., 1977
    Digital Filters, Prentice-Hall, Englewood Cliffs, New Jersey.

Harris, F. J., 1978
    On the use of windows for harmonic analysis with the Discrete
    Fast Fourier Transform. Proc. I.E.E.E., 66, 1, 51-83.

Hayes, S. P., 1980
    The bottom boundary layer in the eastern tropical Pacific.
    Journal of Physical Oceanography, 10, 3, 315-329.

Hinze, J. O., 1959
    Turbulence, McGraw-Hill, New York.

Howroyd, G. C., and P. R. Slawson, 1975
    The characteristics of a laboratory produced turbulent Ekman layer.
    Boundary Layer Meteorology, 8, 201-219.

Käse, R. H., 1979
    Calculations of the energy transfer by the wind to near-inertial
    waves. Deep-Sea Research, 26, 2A, 227-232.

Klebanoff, P. S., 1954
    National Advisory Commission. Aeronautical Technical Notes,
    No. 3178.

Koopmans, L. H., 1974
    The Spectral Analysis of Time Series, Academic Press, New York.

Kovasznay, L. S., V. Kibens, and R. N. Blackwelder, 1970
    Large scale motion in the intermittent region of a turbulent
    boundary layer. Journal of Fluid Mechanics, 41, 2, 283-325.

Kundu, P. K., 1976
    An analysis of inertial oscillations observed near Oregon coast.
    Journal of Physical Oceanography, 6, 6, 879-893.

Leaman, K. D., 1976
    Observations on the vertical polarization and energy flux of near-
    inertial waves. Journal of Physical Oceanography, 6, 894-908.

Lettau, H., 1950
    A re-examination of the "Leipzig Wind Profile". Tellus, 2,
    125-129.

Lighthill, J., 1978
    Waves in Fluids, Cambridge University Press.

Lilly, D. K., 1966
    On the instability of Ekman boundary layer flow. Journal of
    Atmospheric Science, 23, 481, 494.

McComas, C. H., 1977
    Equilibrium mechanisms within the oceanic internal wave field.
    Journal of Physical Oceanography, 7, 836-845.

McCullough, J. R., 1975
    Vector averaging current meter speed calibration and recording
    techniques. Woods Hole Oceanographic Institution Technical
    Report WHOI-75-44.

McPhee, M. G., and J. D. Smith, 1976
    Measurements of the turbulent boundary layer under Pack Ice.
    Journal of Physical Oceanography, 6, 696-711.

Millikan, C. B., 1939
    A critical discussion of turbulent flows in channels and circular
    tubes. In: Proceedings of the 5th International Congress on
    Applied Mechanics, Wiley, New York, 386-392

MODE Group, The, 1978
    The Mid-Ocean Dynamics Experiment. Deep-Sea Research, 25,
    859-910.

Müller, P., D. J. Olbers, and J. Willebrand, 1978
    The IWEX spectrum. Journal of Geophysical Research, 83, 479-500.

Munk W., N. Phillips, 1968
    Coherence and band structure of inertial motion in the sea.
    Rev. Geophysics, 6, 447-472.

Munk, W., F. Snodgrass, and M. Wimbush, 1970
    Tides off-shore: Transition from California coastal to deep-sea
    waters. Geophysical Fluid Dynamics, 1, 191-235.

Phillips, O. M., 1955
    The irrotational motion outside a free turbulent boundary.
    Proceedings of the Cambridge Philosophical Society, 51, 220-229.

Phillips, O. M., 1977
    The Dynamics of the Upper Ocean, 2nd Edition, Cambridge University
    Press.

Piat, J-F., and E. J. Hopfinger, 1980
    A boundary layer topped by a density interface. Submitted to
    Journal of Fluid Mechanics.

Priestley, C.H.B., 1959
    Turbulent Transfer in the Lower Atmosphere, University of Chicago
    Press.

Rhines, P. B., 1979
    Geostrophic turbulence. Annual Reviews of Fluid Mechanics, 11, 401-441.

Sarmiento, J., 1978
    A study of the mixing in the deep sea based on STD, Radon-222 and Radium-228 measurements. Ph.D. Thesis, Columbia University.

Schmitz, W. J., Jr., 1976
    Eddy kinetic energy in the deep western North Atlantic. Journal of Geophysical Research, 81, 4981-4982.

Spencer, A., E. D'Asaro, and L. Armi, 1980
    The Benthic Boundary Layer Experiment on the Hatteras Abyssal Plain: Current and temperature observations, Volume XXV. Woods Hole Oceanographic Institution Technical Report WHOI Ref., in preparation.

Townsend, A. A., 1965
    Excitation of internal waves by a turbulent boundary layer. Journal of Fluid Mechanics, 22, 241-252.

Townsend, A. A., 1976
    The Structure of Turbulent Shear Flow, Cambridge University Press, Cambridge, U.K.

Turner, J. S., 1973
    Buoyancy Effects in Fluids, Cambridge University Press, Cambridge, U.K.

Weatherly, G. L., 1972
    A study of the bottom boundary layer of the Florida Current. Journal of Physical Oceanography, 2, 1, 54-72.

Weatherly, G. L., and P. P. Niiler, 1974
    Bottom homogeneous layers in the Florida Current. Geophysical Research Letters, 1, 7, 316-319.

Weatherly, G. L., and P. J. Martin, 1978
    On the structure and dynamics of the oceanic bottom boundary layer. Journal of Physical Oceanography, 8, 4, 557-570.

Weatherly, G. L., S. L. Blumsack, and A. A. Bird, 1980
    On the effect of diurnal tidal currents in determining the thickness of the turbulent Ekman bottom boundary layer. Journal of Physical Oceanography, 10, 2, 297-300.

Weatherly, G. L., and M. Wimbush, 1980
    Near-bottom speed and temperature observations on the Blake-
    Bahama Outer Ridge. Journal of Geophysical Research, 85,
    C7, 3791-3792.

Wimbush, M., and W. Munk, 1970
    The benthic boundary layer, The Sea Vol. 4, Part 1, Wiley, New
    York, 731-758.

Wunsch, C., 1976
    Geographical variability of the internal wave field: A search
    for sources and sinks. Journal of Physical Oceanography, 6,
    4, 471-485.

Yaglom, A. M., 1979
    Similarity laws for constant-pressure and pressure-gradient
    turbulent wall flows. Annual Reviews of Fluid Mechanics, 11:
    505-540.